# Responses to reviewer 1

We thank the reviewer for the insightful comments and advices. We have implemented, modified and corrected the text according to your comments and suggestions in the revised version. The followings are our point-by point replies. For convenience, your original comments are in Italic and the words marked by red indicate the modified contents from the first revised manuscript.

Major comments

*1) It is valuable to show that this model has reached a quasi- equilibrium state. However, I think this is somewhat overemphasized in the current form. The authors mentioned that their strategy is to tune parameters in a coupled model framework, while it should be cautious that the coupled model will eventually obtain a near-zero TOA radiation balance after a certain period of integration no matter how big the initial imbalance is. Therefore, the results (Fig. 2-5) are not quite surprising/informative.*

*Further, the TOA radiation balance (including OLR in Fig. 6) is strongly coupled to the boundary layer SST. For a fair comparison with observation and other models, the AMIP results with prescribed observed SST should be presented as well. The observed precipitation and OLR are also under current climate not from PI.*

We verified the parameter tuning in the AMIP framework after testing them in the coupled model. The AMIP result shows the simulated precipitation, TOA energy and cloud radiative effects are all realistic. In view of the large number of figures that need to be presented, we did not show these figures, but we plan to present the AMIP and historical simulation results later in a separate paper.

*2) Following comment #1, I think some AMIP simulation results are desired, which can be directly compared to observation and also very helpful to understand the coupled model behaviors.*

Thank you for your good comment. We have implemented more figures (see reply to your point 3) and to avoid excessive lengthy manuscript we will present the AMIP result in other paper.

*3) Besides the time evolution of the variables shown in this paper, many other fields are even more important to show so as to have a more complete assessment of the model's*

*performance, such as atmospheric and oceanic circulation, land surface temperature,*
*annual cycle, diurnal cycle and so on.*

Thank you for your good comment. The reviewer #2 also pointed the same problem, so we add the TOA shortwave radiation, cloud radiative effect, zonal mean temperature, zonal wind, specific humidity and sea ice simulation in the manuscript.

**Minor comments:**

*4) Line 73-83: Several statements are not well supported from this paper. The authors should show some figures and cite the results in previous publications. Line 77: 2W/m2 is also from PI coupled run?*

Thanks for your comments. We the revised the context and also added a reference in this section. The line 73-83 is changed to as follows:

"However, the previous model versions have no vegetation dynamics and cannot be used to study carbon cycle (Cao et al. 2015); in addition, the response of the coupled system to carbon dioxide forcing was over-sensitive; and the poorly resolved vertical layers prevented accuarte simulation of stratospheric phenomena as well as upper tropospheric jet stream. They have large land surface temperature biases and a severe double ITCZ syndrome."

Yes, the 2 W m$^{-2}$ TOA energy imbalance is from the PI experiment of NESM v1, while we didn't show the figure here.

*5) Line 195: 'longitudinal' to 'horizontal'?*
Done.

*6) Line 233-235: Most of current climate models have the initial drift issue that is also relevant to the ocean models. Whether this version of NESM3 has the initial drift problem during the spin up period?*
Yes, both the initial and the current versions the NESM v3 model have the initial drift problem during the spin up period, while the initial version produced much colder global surface temperature after reaching its quasi-equilibrium state.  The PI results in this study are excluded the 400 years coupled model spin up integration.

*7) Line 254-257: I do not understand how these parameters are tuned in a coupled model to obtain a 'better' (near-zero) net global mean heat flux budget. The TOA imbalance will decrease with time and eventually will be close to zero. See my major comment #1.*

Thanks for your comments. The tuned parameters would affect the cloud radiative effect, so that the model TOA energy balance could be changed. For example, the increase of ice crystal falling speed will decrease the cloud top height and decrease the OLR. Therefore, it decreases the TOA energy imbalance. We agree with you that the TOA energy imbalance will decrease with model integration extension. But, most of CMIP5 models show that global mean temperature has a linear trend around 0.02K 100y$^{-1}$ in their PI experiments (Gupta et al. 2013), while the energy analysis show that the TOA energy imbalance is close to 1 W m$^{-2}$ (Fig.3 Fig4 and Table 3 in Wild et al. 2013). To balance the TOA energy, the coupled model may need thousands of years integration. It is hard to do so in our modeling center, so that we tuned the model parameter to decrease the TOA energy imbalance. This is also accepted by other modeling center (e. g. Bentsen et al. 2013; Kay et al. 2016).


*8) Line 262-264: statement without figure support.*

Thanks for your comments. We provided the SST of the original version here. The global averaged annual mean SST is 18.2 °C, which is close to the HadISST in the period of 1979-2009 (18.5 °C). However, the bias pattern shows large cold biases over the NH high latitude where covered by the extensive sea ice.
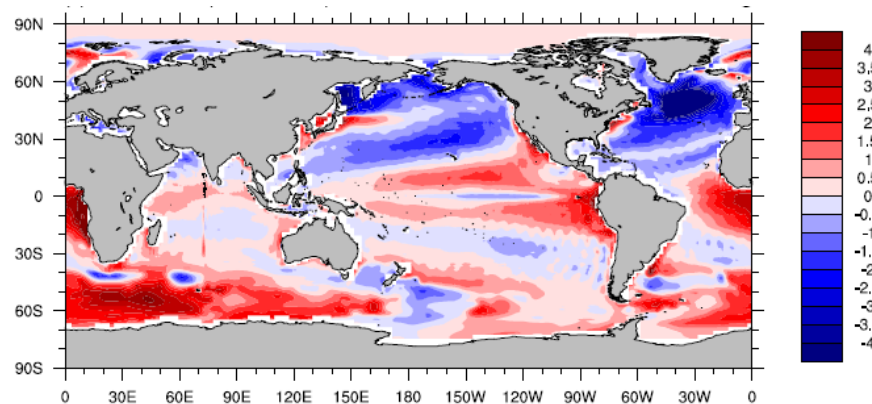


Figure 1 The model SST bias respect to HadISST average from 1979-2008.


*9) Line 272: what are the default configurations?*

Thanks for your comments. We decreased all the albedo parameters by 0.05. That means the visible and near-infrared for sea ice and snow are tuned from 0.78, 0.36, 0.98 and 0.70 to 0.73, 0.31, 0.93 and 0.65, respectively. We add the description in the manuscript as following: "The visible and near-infrared albedos are set to 0.73, 0.31 for ice greater than 0.3 m, and the corresponding cold snow albedos are 0.93 and 0.65, respectively. Those values are slightly smaller than the corresponding default configurations, which are 0.73, 0.31, 0.93, and 0.65 respectively."

*10) Line 290: how does the increased deep convective entrainment and convective mass flux induce the reduced zonal wind stress and cold tongue biases? Through convective momentum transport? It should be cautious that entrainment rate is one parameter that affects nearly every aspect of the parameterized convection. Again, the tuning of these parameters should be tested in AMIP simulations before applying to the fully coupled model simulations.*

Thanks for your comments. When the entrainment rate is increased, convection is suppressed and shallow or congestus clouds are increased, which reduces vertical temperature gradient in the middle-upper troposphere. The decreased vertical temperature gradient increases subsidence in the cold tongue region. These prevent occurrence of deep convection there, resulting in a reduced wind stress and cold tongue SST bias. (e.g. Watanabe et al. 2011).

*11) L306: What is 'modern'?*
The ocean model forcing is from 2000s climatological mean. We changed the 'modern' to '2000s' in the manuscript.
"The ocean component model is spun up with 2000s' atmospheric and sea ice climatological forcings, … "

*12) Line 345-346: I assume that the net fluxes at TOA and surface are downward positive. The difference suggests that the atmosphere loses energy rather than gain energy, right? I think this is likely due to the dynamic core in the atmosphere model.*
Thanks for your comments. Yes, we considered the downward energy flux is positive. In the NESM v3 model, the net solar radiation at TOA is larger than OLR. That means there is a

positive energy imbalance over TOA, which is considered as the anomaly heating. So that we concluded the positive TOA imbalance as the Earth system gains energy. Yes, the artificial energy between TOA and surface is likely due to the dynamic core. And we revised the context correspondingly:

"This problem is found also in the AMIP experiment and it probably due to the energy non-conservation in the model dynamical core."

*13) L379: I think this model tends to underestimate the AMOC strength (14.8 Sv).*

Yes, compare to observations, the model is underestimated the AMOC strength. We added the observational value and revised the manuscript correspondingly.

"The mean strength of AMOC is 14.8 sv, which is underestimated comparing to the modern observational value of 18.5 sv (Cunningham et al. 2007)."

*14) Figure 10, which 10 CMIP5 models? Whether these 10 models are representative of the CMIP5 models (more than 40)?*

Thanks for your comments. We deleted the 10 CMIP5 models' MME in Fig. 10 and directly compared it with other results (e. g. Andrews et al. 2012).

Andrews, T., Gregory, J. M., Webb, M. J., Taylor, K. E.: Forcing, feedbacks and climate sensitivity in CMIP5 coupled atmosphere-ocean climate models. Geophysical Research Letters, 39(9), 2012.

*15) Line 407-417: Comparison of the coupled model to observation is misleading, as the OLR depends on SST (Fig. 7), and the OLR is likely to be very different from its corresponding AMIP simulation. How about the net TOA radiation bias pattern, and the shortwave absorption pattern that largely represents the cloud simulation in this model? Line 431-434: the formation of the double ITCZ is very complicated and the convective parameterization is only one of them.*

Thanks for your comments. We added the TOA shortwave radiation and cloud radiative effect in Fig. 6-9. We agree with you that the formation of the double ITCZ is very complicated. We have no intention to discuss the double ITCZ problem here. We revised the context and add some recently research on the double ITCZ problem. "However, the so-called double-ITCZ precipitation bias exists in the Pacific Ocean and Atlantic Ocean, which is partially linked to

simulated TOA shortwave radiation bias (Xiang et al. 2017) and the insufficient stratocumulus clouds over the eastern Pacific (Bacmeister et al. 2006, Song and Zhang 2009)."

*16) Line 452: fresh water bias?*

Yes, it is fresh water bias. We revised in the context. "Previous studies pointed out that the fresh water bias over high latitudes of North Atlantic can weaken ocean convection,"

*17) Line 508: is the positive shortwave clear sky feedback due to ice-albedo feedback?*

Thanks for your comments. The positive shortwave clear sky feedback includes the ice/snow-albedo feedback and also the shortwave contribution of water-vapor feedback (Andrews et al. 2012) .

Andrews, T., Gregory, J. M., Webb, M. J., Taylor, K. E.: Forcing, feedbacks and climate
      sensitivity in CMIP5 coupled atmosphere-ocean climate models. Geophysical Research
      Letters, 39(9), 2012.

*18) Line 512-514: I do not understand how this is consistent with the conclusion derived from the CMIP5 models?*

Sorry for the confusion. The ECS of NESM v3 model is 10% higher than the CMIP5 MME. The reason maybe the positive cloud radiative effect (CRE) as shown in Fig 12. And the CMIP5 model results suggested the positive CRE model tends to have large ECS (Andrews et al. 2012) .

*19) Line 539-549: It is better to discuss the TCR in observations that is about 1.3-1.7K (et al., Otto et al. 2013; Richardson et al.2016). The increased stratiform clouds through the tuning efforts tend to contribute to the overestimated TCR in this model. This deserves some discussion.*

Thanks for your comments.  According to *Richardson et al. (2016)* the CMIP5 model shows consistent TCR with modern observational results. The TCR of NESM v3 model is larger than the CMIP5 model MME, and it would be larger than the observational estimation (*Richardson et al. 2016*). In our model tuning cycle, the TCR or ECS aren't our first priority, so that we consider the tuning is acceptable when the TCR isn't too far from the CMIP5 MME (e. g. larger than 90% of models) Yes, the model tuning would affect the ECS and TCR as discussed in Sherwood et al. (2014).

Sherwood, S. C., Bony S., Dufresne J-L.: Spread in model climate sensitivity traced to atmospheric convective mixing. Nature, 505,37-42, 2014.

*20) Line 581:The acronym 'SWT' represents 'Sea Water Temperature'?*

Thanks for your comments. It should be "Sea Water Salinity". We changed the SWT to SWS in Line 581. Sorry for the confusion.

"The fresher SSS has no significant influence on SWS. After the spin up, the global mean SSS and SWS have no appreciable trends although the SSS is fresher than the observed counterpart."

*21) Line 595: what do you mean 'slightly'? Better to quantify and compare to other CMIP5 models.*

Our model is suffered the double ITCZ problem and we deleted the word 'slightly'. We will quantify the double ITCZ problem in our historical simulation later.

*22) For OLR, SST, precipitation, please show their global mean value and also the RMSE.*

We added the values in the figures.

*23) Some places require references: Line 397, Line 453, Line 514, Line 522.*

We added the corresponding references as follows.

"This is in part due to the thinner cloud optical depth in the simulated low-level cloud and shallow mixed layer depth over the Southern Ocean (Sterl et al. 2012)."

"Previous studies pointed out that the fresh water bias over high latitudes of North Atlantic can weaken ocean convection, so that weaken the AMOC (Rahmstorf 1995)."

"It could be the reason of slightly high ECS of NESM v3 since the CMIP5 model results suggested that the GCM with higher sensitivity is associated with a positive CRE feedback (Andrews et al. 2012)."

"The most pronounced warming is seen over the Arctic region where sea ice albedo feedback dominates (Screen and Simmonds 2010)."

*24) The version 2 of NESM needs some discussion. Whether there is substantial code difference from v1? If not, I think the current version should be called v2 rather than v3.*

Thanks for your comments. The version 2 of NESM model is based on the v1 model with improved atmospheric internal modes after convective parametrization modification and tuning. It is aimed at developing to a seasonal prediction system. For this purpose, we consider the seasonal prediction version as v2 and the current version as v3.

# Response to reviewer 2

We thank the reviewer for the insightful comments and advices. We have implemented, modified and corrected the text according to your comments and suggestions in the revised version. The followings are our point-by point replies. For convenience, your original comments are in Italic and the words marked by red indicate the modified contents from the first revised manuscript.

Major comments:

*1) I suggest adding figures for annual mean geographical distribution of TOA shortwave, TOA shortwave cloud radiative effect, TOA longwave cloud radiative effect, and surface air temperature over land. Readers would be interested in observation, model results, and model biases for these variables.*

Thanks for your comments. We have added the figures in the revised manuscript according to your suggestions.

*2) I suggest adding figures for geographical distribution of sea ice extent in March and September. Readers would be interested in observation and model results.*

Thanks for your comments. We have added the figures in the revised manuscript as you suggested. We compared the February sea ice concentration following the CMIP5 suggestion instead of March, and the results are similar.

*3) I suggest adding figures for zonal annual mean, latitude-pressure cross section of zonal wind, temperature, and specific humidity.*

Thanks for your comments. We have added the figures in the revised manuscript according to your suggestions.

*4) I suggest adding a table that summarizes global annual mean values for TOA radiation (net, shortwave, longwave, cloud radiative effect), SAT, and precipitation with respect to the model and observation.*

Thanks for your comments. We have added the table in the revised manuscript.

*Minor comments:*

*5) P.3 L.55 "Project" Programme?*

It is Programme. We revised in the context.

"the World Climate Research Programme (WCRP)"


*6) P.6 L.127 "pseudo wavelengths" Please explain the definition of the pseudo wavelengths.*

We added the explanation in the context.

"The upward and downward irradiance are calculated over a predetermined number of pseudo wavelengths, or g-points, an approach is usually referred to as the correlated-$k$ method, where $k$ denotes absorption and $g$ indexes the cumulative distribution of absorption within a band (Zdunkowski et al. 1980)."

Zdunkowski, W. G., Welch, R. M. and Korb, G. J. : An investigation of the structure of typical two-stream methods for the calculation of solar fluxes and heating rates in clouds. Beitr. Phys. Atmos., 53, 147–166, 1980.


*7) P.6 L.128 "time step for radiation scheme" "Frequency of radiation calculation" maybe a more appropriate expression , because the word "time step" has a different meaning.*

We changed the *"time step for radiation scheme"* to *"Frequency of radiation calculation"* as you indicated.

"The frequency of radiation calculation is two hours."


*8) P.7 L.129 "kinetic energy scheme" Reference to the paper describing the turbulence scheme would be helpful.*

Thanks. We added the reference in the manuscript as followings:

"The turbulent transport employs the turbulent kinetic energy scheme (Brinkop and Reockner 1995),"

Brinkop, S. and Roeckner, E.: Sensitivity of a general circulation model to parameterizations of cloud-turbulence interactions in the atmospheric boundary layer. Tellus, 47A,197–220, 1995.

*9) P.7 L.134 "stratiform cloud scheme" Reference to the paper describing the cloud scheme would be helpful.*

We added the reference in the manuscript as followings:

"a cloud microphysical scheme, and a diagnostic cloud cover scheme (Sundqvist et al. 1989)."

Sundqvist, H., Berge, E. and Kristjansson, J. :Condensation and cloud parameterization studies with a mesoscale numerical weather prediction model. Mon. Wea. Rev., 117, 1641–1657, 1989.


*10) P.7 L.137 "Lott and Miller 1997" I cannot find the paper in the reference list.*

We added it in the reference list.

"Lott, F. and Miller, M. J.: A new-subgrid-scale orographic drag parameterization: Its formulation and testing. Quart. J. Roy. Meteor. Soc., 123, 101–127, 1997."


*11) P.9 L.174 "Hunck and Dukowicz 2002" I think the correct spelling is "Hunke". I cannot find the paper in the reference list.*

We revised the manuscript as follows:

"The sea ice deformation is computed basing on the Elastic-Viscous-Plastic scheme (Hunke and Dukowicz 2002) with"

*And*

"Hunke, E. C, and Dukowicz, J. K.: The elastic–viscous–plastic sea ice dynamics model in general orthogonal curvilinear coordi- nates on a sphere—Incorporation of metric terms. Mon. Wea. Rev., 130, 1848–1865, 2002."


*12) P.10 L.195 "longitudinal" Horizontal?*

Yes, it should be "horizontal". We change it to "horizontal" in the context.

"The resolution of ocean model is higher than atmospheric model with the horizontal resolution of 1° ×1° in sr and 2° ×2° in lr version."


*13) P.10 L.206 "Clouds and the Earth's ... and Filled" Please explain what variables in this data set are used for the model evaluation (TOA radiation).*

We added the data information in the context.

"(3) the radative fluxes from edition 2.8 of the Clouds and the Earth's Radiant Energy System- Energy Balanced and Filled (CERES-EBAF, Loeb et al. 2009);"


*14) P.10 L.208 "World Ocean Atlas 2009" Please explain what variables in this data set are used for the model evaluation.*

We added the data information in the context.

"(4) the ocean temperature and salinity from World Ocean Atlas 2009 (WOA09) (Locarnini et al. 2010)."


*15) P.17 L.352 "14.2C" Fig.3 shows that the mean surface air temperature is 14.9C.*

We revised the number in the context as follows:

"The mean value of the near surface air temperature (TAS) is 14.9 ℃ in the entire period, and the linear trend of TAS is 0.00214 ℃ (100yr)$^{-1}$."


*16) P.17 L.353 "-0.0021 C(100yr)^-1" Fig.3 shows that the linear trend of TAS is +0.00214 C(100yr)^-1.*

We revised the number in the context as follows:

"The mean value of the near surface air temperature (TAS) is 14.9 ℃ in the entire period, and the linear trend of TAS is 0.00214 ℃ (100yr)$^{-1}$."


*17) P.17 L.355 "-0.016 C(100yr)^-1" Fig.3 shows that the linear trend of land surface temperature is -0.00984 C(100yr)^-1.*

We revised the number in the context as follows:

"The linear trend of land surface temperature is -0.00984 ℃ (100yr)$^{-1}$."

*18) P.17 L.357 "-0.0073 C(100yr)^-1" Fig.3 shows that the linear trend of SST is +0.00731 C(100yr)^-1.*

We revised the number in the context as follows:

"The negligible SST trend (0.00731℃ (100yr)$^{-1}$)"

*19) P.18 L.379 "the modern observational value" Readers would be interested in how large is the observational value.*

We revised the manuscript as follows:

"The mean strength of AMOC is 14.8 sv, which is underestimated comparing to the modern observational value of 18.5 sv (Cunningham et al. 2007)."

*20) P.18 L.395 "recent decade's observation" Readers would be interested in how large is the recent decade's observation.*

We deleted this sentence since the sea ice coverage is compared with the observation in Fig. 17-18.

*21) P.19 L.410 "within the range of uncertainty among different observations" Readers would be interested in what observations are used to estimate the uncertainty range. ?*

Thanks for your comment. Loeb et al. (2009) compared the OLR from several observational data suggested the OLR can be vary from 235.2 W m$^{-2}$ to 240.4 W m$^{-2}$. We added the reference in the manuscript, so that the readers can be referred to the literature.

"differences are within the range of uncertainty among different observations (Loeb et al. 2009)."

Loeb, N. G., B. A. Wielicki, D. R. Doelling, G. L. Smith, D. F. Keyes, S. Kato, N. Manalo-Smith, and T. Wong, 2009: Toward optimal closure of the earth's top-of-atmosphere radiation budget. J. Climate, 22, 748–766

*22) P.22 L.478 "quadrupling atmospheric carbon dioxide" Doubling?*

Sorry for the confusion. It should be "doubling". We revised as follows: " The ECS is regarded as the global equilibrium TAS change in response to the <span style="color:red">doubling</span> atmospheric carbon dioxide concentration."

*23) P.22 L.479 "product of the radiative forcing and the climate feedback parameter" Ratio of the radiative forcing to the climate feedback parameter?*

Yes. It is the ratio of the radiative forcing to the climate feedback parameter. We changed the description in the context as follows:" It is also indicated by the <span style="color:red">ratio of the radiative forcing to the climate feedback parameter</span>."

*24) P.23 L.494 "climate feedback parameter is considered as a constant" There are increasing number of evidence that climate feedback changes according to the surface temperature pattern (e.g., Andrews et al. 2015, J.Climate). Therefore, the sentence here could be refrased as "if we approximate the climate feedback parameter as a constant".*

Thanks for your comment. We changed the description as you indicated. "Since the radiative forcing is logarithmically related to the carbon dioxide concentration <span style="color:red">if we approximate the climate feedback parameter as a constant (Hansen et al. 2005)</span>,"

*25) P.40 Figure 1 "JSBACH Dyn. Veg." The main text (L.114) explains that the JSBACH is a land surface model which is not equivalent to the parameterization for the dynamic vegetation.*

Yes, it is the land surface model, and we replotted the Figure 1.

*26) P.41 Figure 2 The legend refers to the labels (a) and (b), which are not shown in the figure.*

Thanks for your comment. We revised the figure 2 legend with more clear indication.

*27) P.43 Figure 4 "sea water salinity", "sea water temperature" Are these volume-mean values for the full-depth global ocean?*

Yes, the sea water salinity and sea water temperature are both representing the volume-*mean values for the full-depth global ocean*. We added the explanation of sea water salinity and sea water temperature in the context and figure caption.

*28) P.45 Figure 6 "CERES" Which edition of the CERES data is used?*

The edition 2.8 of the CERES data is used. We added the description in the figure caption. "The observed OLR filed was derived from the edition 2.8 of Clouds and the Earth's Radiant Energy System (CERES) dataset (Loeb et al. 2009)."

*29) P.51 Figure 12 It is difficult to read the numbers and characters in the figure because they are small.*

Thanks for your comment. We replotted the Figure 12 with better quality.

# The NUIST Earth System Model (NESM) version 3:

# Description and preliminary evaluation

Cao, Jian[1,2], Bin Wang[1,2,*], Young-Min Yang[2], Libin Ma[1,2], Juan Li[1,2], Bo Sun[1,2], Yan Bao[1,2], Jie He[1,2] and Xiao Zhou[2]

1. Earth System Modeling Center, the Nanjing University of Information Science and Technology, Nanjing 210044, China

2. China-US joint Atmosphere-Ocean Research Center and International Pacific Research Center, University of Hawaii, Honolulu Hawaii 96822 USA

August 21 2017

Submitted to Geoscientific Model Development

*Corresponding author: Bin Wang, wangbin@hawaii.edu

18          **Abstract**

19      The Nanjing University of Information Science and Technology Earth System Model

20   version 3 (NESM v3) has been developed, aiming to provide a numerical modeling

21   platform for cross-disciplinary earth system studies, project future Earth's climate and

22   environment changes, as well conduct subseasonal-to-seasonal prediction. While the

23   previous model version NESM v1 simulates well the internal modes of climate variability,

24   it has no vegetation dynamics and suffers considerable radiative energy imbalance at the

25   top of the atmosphere and surface, resulting in large biases in the global mean surface air

26   temperature, which limit its utility to simulate past and project future climate changes.

27   The NESM v3 upgraded the atmospheric and land surface model components and

28   improved physical parameterization and conservation of coupling variables. Here we

29   describe the new version's basic features and how the major improvements were made.

30   We demonstrate the v3 model's fidelity and suitability to address the global climate

31   variability and change issues. The 500-year pre-industrial (PI) experiment shows

32   negligible trends in the net heat flux at the top of atmosphere and the Earth surface.

33   Consistently, the simulated global mean surface air temperature, land surface temperature

34   and sea surface temperature (SST) are all in a quasi-equilibrium state. The conservation

35   of global water is demonstrated by the stable evolution of the global mean precipitation,

36   sea surface salinity (SSS) and sea water salinity. The sea ice extents (SIEs), as a major

37   indication of high latitude climate, also maintain a balanced state. The simulated spatial

38   patterns of the ~~mean outgoing longwave radiation~~energy states, SST, precipitation, SSS

39   fields are realistic, but the model suffers from a cold bias in the North Atlantic, a warm

40   bias in the Southern Ocean and associated deficient Antarctic sea ice area, as well as a

2

41     delicate sign of the double ITCZ syndrome. The estimate radiative forcing of quadrupling

42     carbon dioxide is about 7.24 $Wm^{-2}$, yielding a climate sensitivity feedback parameter of -

43     0.98 $Wm^{-2}K^{-1}$, and the equilibrium climate sensitivity is 3.69 K. The transient climate

44     response from the ~~1pct/year~~1% $yr^{-1}$ $CO_2$ (1pctCO2) increasing ~~$CO_2$~~ experiment is 2.16 K.

45     The model's performance on internal modes and responses to external forcing during the

46     historical period will be documented in an accompanying paper.

47

## 48   **1. Introduction**

49     Large internal variability of the Earth climate system involves complex feedbacks

50     among the atmosphere, hydrosphere, cryosphere, land surface and biosphere. As an

51     essential tool to reproduce the Earth's paleoclimate evolution, project future climate

52     change, and understand the mechanisms governing climate variability and change, the

53     Climate ~~system~~ System ~~model~~ Model (CSM) and Earth System Model (ESM) have

54     attracted greatest attention of the scientific community. Starting from 1995, the World

55     Climate Research ~~Project~~ Programme (WCRP) established and regularly organized

56     Coupled Model Intercomparison Projects (CMIPs) (Meehl et al. 2000). The CMIP has

57     not only stimulated the coupled model development, facilitated model output validation,

58     deepened scientific understanding of the Earth climate change, but also provided

59     scientific guidance for the Intergovernmental Panel on Climate Change (IPCC).

60     The first generation of Nanjing University Information Science and Technology

61     (NUIST) Earth System Model (NESM v1, Cao et al 2015) was established with the

62     atmospheric model ECHAM v5.3, ocean model NEMO v3.4, sea ice model CICE v4.1

63 and coupler version 3 of the Ocean-Atmosphere-Sea-Ice-Soil Model Coupling Toolkit

64 (OASIS3.0-MCT). It was targeted to meet the demand of seamless climate prediction,

65 simulate the past and project future climate change, and study of climate variability of

66 high-impact weather events. The performances of NESM v1 model have been evaluated

67 (Cao et al. 2015) and further developed into a seasonal prediction system (NESM v2) by

68 modification and tuning of convective parameterization and cloud mircophysics. The

69 NESM v1 was also used to study the changes in Last Glacial Maximum climate and

70 global monsoon, demonstrating reasonable model response with external forcing (Cao et

71 al. 2016). Numerical experiments with NESM v2 were conducted to confirm the sources

72 of predictability of the Indian summer monsoon rainfall (Li et al. 2016) and the winter

73 extremely cold days in East Asia (Luo and Wang 2018 ~~submitted~~).

74 However, the previous model versions have no vegetation dynamics in the land

75 surface model and cannot be used to study carbon cycle (Cao et al. 2015); and the

76 response of the coupled system to carbon dioxide forcing was over-sensitive. ~~Another~~

77 ~~serious problem is the relatively large energy imbalance at the TOA and surface, both~~

78 ~~have an imbalance of ~2Wm$^{-2}$ in PI experiment. There are also significant biases in the~~

79 ~~TOA net solar radiation and OLR.~~ Meanwhile, the poorly resolved vertical layers

80 prevented correct simulation of stratosphere phenomena as well as high-level jet stream.

81 They have large land surface temperature biases and a severe double ITCZ syndrome.

82 ~~The SST over high latitude North Atlantic is excessively cold, the strength and extent of~~

83 ~~the Atlantic Meridional Overturning Circulation (AMOC) is underestimated, the~~

84 ~~Southern Ocean is too warm, and the sea ice coverage over the Antarctic is substantially~~

85 ~~deficient.~~

86    Facing the forth coming CMIP6, a more comprehensive and improved Earth System

87    Model is needed to perform CMIP6 experiments and to address forcing-related scientific

88    questions. For this purpose, we have developed a new version of NESM v3.~~0~~. The major

89    changes include an updated land surface model with dynamic vegetation and carbon

90    exchange, improved shortwave and longwave radiation schemes, new schemes for

91    description of aerosols and computation of surface albedo, increased vertical resolution of

92    the atmosphere model and horizontal resolution of the ocean and sea ice models.

93    As a registered model of CMIP6, the NESM_v3.~~0~~ model is to be used to perform the

94    DECK simulation, historical experiment, and some endorsed MIPs following the CMIP6

95    experiment design protocol (Eyring et al. 2016). The selected MIPs include: Detection

96    and Attribution Model Intercomparison Project (DAMIP), Scenario Model

97    Intercomparison Project (ScenatioMIP), Decadal Climate Prediction Project (DCPP),

98    Global Monsoons Model Intercomparison Project (GMMIP), Paleoclimate Modelling

99    Intercomparison Project (PMIP), Volcanic Forcings Model Intercomparison Project

100   (VolMIP), and Geoengineering Model Intercomparison Project (GeoMIP).

101   This paper documents the main features of the NESM v3, the major model

102   improvement, and the preliminary evaluation of model's long term integration and

103   climate sensitivity to carbon dioxide forcing. In the new version 3, the energy balance is

104   substantially improved, including the net shortwave radiation and outgoing longwave

105   radiation and their balance. The biases are in a few tenths $Wm^{-2}$ and the trends are

106   negligible. This is demonstrated by the PI experiment with perpetual unchanged forcing,

107   and the climate sensitivity is tested through the abruptly quadrupling $CO_2$ experiment and

108   1pctCO2 ~~gradually 1% $CO_2$/year increase~~ experiment.

109 The model description is presented in Section 2, which is followed by the coupled

110 model tuning strategy (Section 3). In Section 4 and 5, the model long-term stability and

111 the mean climate states are evaluated. Section 6 examines the model climate sensitivity in

112 perturbing atmospheric carbon dioxide concentration. The last section presents a

113 summary.

## 2. Model description and validation data

114

115 The NESM v3 consists of the ECHAM v6.3 atmospheric model, which directly

116 coupled with JSBACH land surface model, the NEMO v3.4 ocean model, the CICE v4.1

117 sea ice model; and the OASIS3-MCT_3.0 coupler. The model structure is illustrated in

118 Fig.1, and brief description of each component model follows.

### 2.1 Atmosphere and land surface model

119

120 The ECHAM v6.3 and JSBACH model are originally adopted from the Max Planck

121 Institute ECHAM serial model. A brief introduction will be presented here; the detailed

122 documentation can be found in Stevens et al. (2012) and Giorgetta et al. (2013). The

123 ECHAM v6.3 employs the spectral/finite-difference dynamic core for adiabatic process.

124 Calculations of all parameterizations and non-linear terms are transferred to Gaussian

125 grids. A hybrid sigma-pressure coordinate system (Simmons et al. 1999) is used in the

126 vertical discretization. The shortwave and longwave radiation schemes are both from the

127 Rapid Radiation Transfer Model for General Circulation model's (RRTM-G) scheme

128 (Iacono et al. 2008), which takes the two-stream approach. The upward and downward

129 irradiance are calculated over a predetermined number of pseudo wavelengths, or g-

130 points, an approach is usually referred to as the correlated-$k$ method, where $k$ denotes

absorption and *g* indexes the cumulative distribution of absorption within a band (Zdunkowski et al. 1980). The ~~time step for~~frequency of radiation calculation ~~radiation scheme~~ is two hours. The turbulent transport employs the turbulent kinetic energy scheme (Brinkop and Reockner 1995), and the surface fluxes are calculated using the bulk-exchange formula which is based on Monin-Obukhov similarity theory. The model parameterizes shallow, deep and midlevel convection separately. The deep convection is based on mass-flux framework developed by Tiedtke (1989) and further improved by Nordeng (1994). Currently, the shallow, deep and midlevel convection are parameterized by the Tiedtke, Nordeng, and Tiedtke scheme, respectively. The stratiform cloud scheme contains the prognostic equations for the vapor, liquid, and ice phase, respectively, a cloud microphysical scheme, and a diagnostic cloud cover scheme (Sundqvist et al. 1989). The ECHAM v6.3 implements the Subgrid Scale Orographic Parameterization scheme (Lott and Miller 1997, Lott 1999) to represent the momentum transport arising from subgrid orograph.

The JSBASH land surface model simulates fluxes of energy, momentum, moisture, and tracer gases between the land surface and atmosphere (Raddatz et al. 2007). The JSBACH model contains a 5-layer soil, a dynamic vegetation scheme and a land albedo scheme. The tiled structure of land surface is divided into eight natural Plant Functional Types (PFTs), four anthropogenic PFTs and two types of bare surface (Brovkin et al. 2013). The dynamic vegetation scheme is based on the assumption that the competition between different PFTs is determined by their relative competitiveness expressed in the annual net primary productivity, as well as natural and disturbance-driven mortality. The surface

153 albedo is calculated at each tile of the land surface for near-infrared and visible range of

154 solar radiation.

## 2.2 Ocean model

156 The ocean component model of NESM_v3 is Ocean PArallelise (OPA), the ocean part

157 of NEMO v3.4 (Nucleus of European Modelling of the Ocean). The primitive equation of

158 ocean model is numerically solved on an orthogonal curvilinear grid. It uses the isotropic

159 Mercator projection south of 20_°N, and a stretched grid north of 20_°N with two poles in

160 Canada and Siberia, which removes the singularity of spherical coordinate in the Arctic

161 ocean and allows the cross polar flow (Madec and Imbard, 1996). The ORCA1

162 configuration of ocean model corresponds to a resolution of 1 degree of longitude and a

163 variable mesh of 1/3 to 1 degree of latitudes from the equator to pole. It has 46 vertical

164 layers which adopts the z-coordinate with partial steps (Adcroft et al., 1997; Bernard et

165 al., 2006). At the ocean surface, the linear free surface method is used (Roullet and

166 Madec, 2000). Advection of tracer uses the total variance dissipations scheme (TVD)

167 (Zalesak, 1979). Horizontal momentum is diffused with a Laplacian operator and 2-D

168 spatially-varying kinematic viscosity coefficient. The vertical mixing of tracer and

169 momentum is parameterized using turbulent kinetic energy scheme. Besides, the lateral

170 diffusion is solved on the neutral direction (Redi, 1982) and includes eddy-induced

171 advective processes (Gent and McWilliams, 1990). The incoming solar radiation is

172 distributed in the surface layers of the ocean using simplified RGB and chlorophyll-

173 dependent attenuation parameters (Lengaigne et al., 2009). The model uses a diffusive

174 bottom boundary layer (Bechmann and Doscher 1997).

## 2.3 Sea ice model

The sea ice model in the NESM v3 is CICE v4.1, which is originally developed at the Los Almos National Laboratory. The model solves dynamic and thermodynamic equations for five categories of ice thickness. The lower bound for the five thickness categories are 0, 0.6, 1.4, 2.4, and 3.6 m, respectively. The sea ice deformation is computed basing on the Elastic-Viscous-Plastic scheme (Hunke and Dukowicz 2002) with the ice strength determined by using the formulation of Rothrock (1975). The ice thermodynamics are calculated at five ice layers corresponding to each thickness category instead of zero-layer thermodynamic option.

## 2.4 Coupling method with OASIS3-MCT

The coupling method is the same as the previous version of NESM v1, and the detail information is described in Cao et al (2015). But the coupler has been upgraded from OASIS3-MCT to OASIS3-MCT_3.0 (Valcke and Coquart 2015), which is a fully parallelized tool for coupled model. The coupler is used to synchronize, interpolate and exchange the coupling fields among the atmospheric, oceanic and sea ice component models. To conserve the exchange coupling fields, the second order conservation interpolation is used in remapping the energy, mass, momentum, and tracers, so to avoid energy, momentum loss and spurious climate drift. The component models are coupled daily.

## 2.5 Configuration

Two subversions are included in the NESM v3, namely the standard-resolution version (sr) and low-resolution (lr) version. In the atmospheric model, the sr and lr

197  versions have a horizontal resolution of T63 and T31, respectively. The T63 corresponds

198  to about 1.9° in meridional and zonal directions. The sr (lr) version has 47 (31) levels in

199  the vertical which extends from the surface up to 0.01 (1.0) hPa. The resolution of land

200  surface model is the same as the atmospheric model. The resolution of ocean model is

201  higher than atmospheric model with the ~~longitudinal~~ horizontal resolution of 1° ×1° in sr

202  and 2° ×2° in lr version. The resolution in the meridional direction is refined to 1/3° and

203  2/3°, respectively, over the tropical region. In the vertical direction, the sr (lr) version has

204  46 (31) vertical layers with the first 15 (9) layers at the top 100 meters. In both sr and lr

205  versions, the sea ice model resolution is about 1° ×1/2° in meridional and zonal directions

206  with four sea ice layers and one snow layer on the top of the ice surface.

207  **2.6 Validation data**

208      To validate the model performance, the following observational data are used: (1) the

209  combined precipitation data of Global Precipitation Climatology Project (GPCP) version

210  2.2 and Climate Prediction Center Merged Analysis of Precipitation (CMAP) (Xie and

211  Arkin, 1997; Lee and Wang, 2014); (2) Hadley Centre Global Sea Ice and Sea Surface

212  Temperature (HadISST), (Rayner et al., 2003); (3) the land surface temperature from

213  CRU-TS-v3.22 (Harris et al. 2014); (4~~3~~) the radiative fluxes from edition 2.8 of the

214  Clouds and the Earth's Radiant Energy System- Energy Balanced and Filled (CERES-

215  EBAF, Loeb et al. 2009); (5~~4~~) the atmospheric zonal wind, temperature and specific

216  humidity from ERA-interim (Dee et al. 2011); (6) ~~–~~the ocean temperature and sanility

217  from World Ocean Atlas 2009 (WOA09) (Locarnini et al. 2010).

218  **3. Model improvement and tuning**

219       Model sub-grid processes are represented by physical parameterizations.

220    Improvement of physical parametrizations and calibration the parameters within the

221    parametrization schemes using constraints obtained from observation, physical

222    understanding or empirical estimation is an integral part of the model development cycle.

223    Our strategy to improve model performance and tuning parameters includes three

224    elements. First, our principle is that the final tuning of all parameters must be conducted

225    using the fully coupled climate model. Second, to efficiently identify the model's

226    weakness and the effects of the tuning, we designed a standard metrics for evaluation of

227    the model's climatology and major modes of variability, which include total of 160 fields

228    covering the climatology of the atmosphere, ocean, land and sea ice, and internal and

229    coupled modes of variability such as Madden-Julian oscillation (MJO), Arctic oscillation

230    (AO), Antarctic Oscillation (AAO), North Atlantic Oscillation (NAO), global monsoon,

231    El Nino-Southern Oscillation (ENSO), Atlantic Meridional Overturning Circulation

232    (AMOC), Atlantic multidecadal Oscillation (AMO), Pacific Decadal Oscillation (PDO),

233    and major teleconnection patterns etc. Result from each tuning experiment is compared

234    with the corresponding observations when they are available or CMIP5 multi-model

235    ensemble means when observations are not available. This assessment process helps to

236    identify the models' major problems and the consequences of the tuning, and to

237    understand how the tuning works. Third, a low-resolution version model, the NESM v3lr,

238    is developed, which allows integration about four times faster than the standard

239    resolution version so that the tuning experiments can get results quickly. Once the tuning

240    is successful in the low-resolution model, similar tuning is applied to the standard

241    resolution version with necessary resolution-dependent adjustment.

242    The initial version of the v3 model has considerable trends in the surface air

243    temperature and SST, which is associated with the reduced net solar radiation and

244    outgoing longwave radiation (OLR), as well as a large energy imbalance at the top of the

245    atmosphere (TOA). The global mean surface air temperature (TAS) and SST was about 1

246    K lower than the observed and suffered a continuing drift. Meanwhile, the sea ice extent

247    and sea ice thickness in both Hemispheres kept increasing in the long-term integration.

248    Our first task was aimed at obtaining a nearly balanced global mean energy at the TOA

249    and surface, as well as a reasonable global mean surface temperature with perpetual pre-

250    industry forcing. This is critical for achieving a stable long-term integration in pre-

251    industry simulation which acts as the benchmark experiment for entry card for CMIP6

252    (DECK) and historical run as well as some other MIPs. Another tuning consideration is

253    the long-term climatology and internal modes of the Earth System in the current climate

254    condition. Efforts are made to minimize the biases in the simulated SST, sea level

255    pressure (SLP), precipitation, zonal mean temperature and wind, ocean mean state (sea

256    surface salinity, mix layer depth etc.) as well as ENSO, global monsoon, and MJO. In

257    addition, the historical evolution of surface temperature is an important measurement of

258    the model's fidelity. This is along with the abrupt quadrupling and gradually increased 1%

259    $yr^{-1}$ $CO_2$ experiments in estimating the model climate sensitivity.

260    The key tuning parameters in the v3 versions are related to the stratiform cloud,

261    cumulus convection, ocean mixing process, and sea ice albedos. Iterative tunings were

262    conducted in the standalone component models with observed/reanalysis forcing and in

263    the coupled model during the PI control run. To achieve a better global mean radiative

264    energy level and a near zero (within a few tenth W $m^{-2}$) net global mean heat flux budget,

265    the parameter calibrations are conducted on the relative humidity threshold that is related

266    to cloud forming process and the estimated cloud cover (Mauritsen et al. 2012). The

267    parameters involved in the cloud microphysics are also tuned, including the accretion of

268    cloud water (ice) to rain (snow), auto-conversion rate of cloud water to rain, and ice

269    crystal and rain drop fall speeds, which are recognized as effective parameters in

270    affecting both short and longwave radiation (Mauritsen et al. 2012, Hourdin et al. 2017).

271    Even with reasonable global mean SST, the model simulated excessive sea ice extent

272    over the Arctic, especially over the Davis Strait, Fram Strait and North Atlantic during

273    winter (figure not shown). The export of sea ice from Davis Strait significantly increases

274    the SST and salinity biases. To mitigate the North Hemisphere sea ice extent bias, the sea

275    ice albedo and ice transport-related parameters were adjusted. Sea ice albedo is one of the

276    most effective tunable parameter to adjust sea ice extent and thickness (Hunck~~ke~~ 2010).

277    The default sea ice albedo parameterization takes into account the radiative spectral band,

278    ice thickness and others. The visible and near-infrared albedos are set to 0.73, 0.31 for ice

279    greater than 0.3_m, and the corresponding cold snow albedos are 0.93 and 0.65,

280    respectively. Those values are slightly smaller than the corresponding default

281    configurations, which are 0.73, 0.31, 0.93, and 0.65 respectively. On the other hand, the

282    sea ice motion is largely driven by the ocean currents, sea surface height gradients and

283    wind stress. The efficiencies of air-ice and ocean-ice drag are important for sea ice

284    transport, as well as sea ice extent during winter and spring (Urrego-Blanco et al. 2016).

285    In this model, the ice surface roughness was decreased and the ocean-ice drag coefficient

286    was increased to decrease the sea ice export over Davis and Fram Strait. This is based on

287    the understanding that the air-ice and ocean-ice drag parametrizations have large

288    uncertainty in the current CICE model.

289       Concerning the internal modes, ENSO and Intraseasonal oscillation (ISO) are

290    recognized as the dominate modes on the interannual and intraseasonal time scale,

291    respectively. They significantly influence the tropical and global climate through

292    atmospheric teleconnections. Much attention was paid to improve the simulation of

293    ENSO and ISO in v3.

294       The ENSO-related SST variability, ENSO phase locking to annual cycle, and the

295    equatorial Pacific cold SST bias are closely related (Ham and Kug 2014). CMIP5 models'

296    results suggested that the models having less cold tongue SST bias reproduce more

297    realistic ENSO phase locking owing to models' simulation of more realistic coupled

298    feedbacks. The change of cloud parametrization has an effect on the mitigation of the

299    clod tongue SST bias, which can lead to an improved ENSO phase locking (Wengel. et al.

300    ~~2017~~2018). In the NESM v3 model, the parameter of deep convective entrainment and

301    convective mass flux above the buoyance layer have been increased which resulted in a

302    reduced cold tongue bias and zonal wind stress over the equatorial Eastern Pacific,

303    removal of the excessive SST variance over the central Pacific, and improved ENSO

304    phase locking.

305       The entrainments in deep and shallow convections are associated with the moisture

306    supply in the free atmosphere. Strong convection plumes can increase the water supply

307    for the formation of stratiform clouds, leading to an increase of stratiform precipitation.

308    The interaction between wave dynamics and precipitation heating is essential for the

309 development and propagation of intraseasonal oscillation (Fu and Wang 2009). The

310 entrainment rates associated with convections are adjusted which allow more stratiform

311 precipitation formed in the coupled model. It strengthens the ISO signal and also

312 significantly enhances the MJO eastward propagation.

## 4. Model stability under fixed external forcing

314 The standalone spin-up of ocean and land states is an efficient method to accelerate

315 the spin up process in the coupled model, especially in the PI control simulation. The

316 ocean component model is spun up with 2000s' ~~modern~~ atmospheric and sea ice

317 climatological forcings, such as radiation, winds, precipitation, sea ice concentration and

318 so on. The offline integration length is 2000 (4000) model years for ocean component of

319 NESM v3sr (v3lr) model. The land surface initial condition is adopted from MPI-ESM-

320 LR model which has active dynamic vegetation and carbon cycle. The initial conditions

321 of the atmospheric and sea ice model in the coupled system used the modern observations.

322 The pre-industry control simulation is performed following the CMIP6 protocol with

323 forcing fixed at the year 1850 or around 1850s. The choice of forcing in ~~time point~~1850

324 or of decadal mean in 1850s ~~forcing~~ is to minimize the initial shock of the ensuing

325 historical simulation. The earth orbital parameters, greenhouse gases, ozone

326 concentration, land surface conditions are fixed at their 1850 values. The solar constant

327 used is the 11 years mean from 1850-1860. The natural tropospheric aerosol and 1850s

328 mean stratospheric aerosol forcing were employed in the coupled system. During the

329 whole PI simulation, there was no land use/land cover change. The coupled model was

330 spun up for 400 years so that the model reached an equilibrium state. After that, a 500

331 years PI simulation is conducted and evaluated in this study.

15

332    One of major purposes of the PI control experiment is to verify the model's stability in

333    the perpetual, unchanged forcing conditions. In this section, emphasis will put on

334    evaluation of the equilibrium state of the top-of-atmosphere (TOA), atmosphere-ocean-

335    sea ice interface to reveal the energy, water, and mass conservation of the whole system.

336    The energy input at the TOA is the major energy source for the Earth System. It is vital to

337    minimize the net energy imbalance at the TOA and surface, which can avoid temperature

338    drift in the system. The major indicators are the land surface temperature and ocean

339    surface temperature; they also work as the direct monitor of system energy conservation.

340    The precipitation is the most important part of global hydrological cycle, which involves

341    the energy exchange, as well as mass exchange among each climate system components.

342    The ocean salinity is sensitive to the state of surface hydrological cycle, land runoff and

343    sea ice melting/formation process. Sea ice extent is a good indicator of sea ice amount in

344    both Arctic and Antarctic regions, and it is sensitive to ocean heat content drift and high

345    latitude energy transfer. To better quantify the climate drifts, linear trends were calculated

346    for all evaluation variables.

347    The time evolution of global mean energy budget at the TOA, Earth surface and ocean

348    surface are shown in Fig. 2. The global mean net shortwave radiation at the TOA

349    averaged over the 500-year integration is 238.55 $W\,m^{-2}$ and the corresponding outgoing

350    longwave radiation (OLR) is -238.39 $W\,m^{-2}$, resulting in a net atmospheric energy gain of

351    0.17 $W\,m^{-2}$. The net heat budget at the TOA shows a negligible decreasing trend of -

352    0.0041 $W\,m^{-2}(100yr)^{-1}$. At the Earth surface, the net energy imbalance is 0.31 $W\,m^{-2}$ in

353    the whole integration period with an insignificant decreasing trend of -0.00576 $W\,m^{-2}$

354    $^{2}(100yr)^{-1}$. The negative trends are shown at both the TOA and surface, indicating the

355   coupled system could lead to a more stable state when the integration extends. Note that

356   there is a difference of 0.14 W_m$^{-2}$ between surface and TOA net energy budget, which

357   means the model atmosphere ~~gains~~ produces artificial energy. This problem is found also

358   in the AMIP experiment and it probably due to the energy non-conservation in the model

359   dynamical core.

360     The trends in the surface temperature indices, namely global mean surface air

361   temperature, land surface temperature and SST, reveal the energy conservation and

362   stability as well as the stability of air-sea-sea ice interaction in the coupled system (Fig.

363   3). The mean value of the near surface air temperature (TAS) is 14.~~2~~9 ℃ in the entire

364   period, and the linear trend of TAS is -0.00214~~0.0021~~ ℃ (100yr)$^{-1}$. This trend is mainly

365   attributed to the land surface temperature rather than SST. The linear trend of land

366   surface temperature is -0.00984 ~~-0.016~~℃ (100yr)$^{-1}$. The slow balance of terrestrial (land)

367   vegetation may be one of the reasons. The global time-mean SST is 17.7 ℃, which is

368   consistent with the observation measured during the decade of ~~1850~~1870-~~1860~~1880. The

369   negligible SST trend (-0.0073~~1~~℃ (100yr)$^{-1}$) indicates the global mean SST reached a

370   quasi-equilibrium state. As the most important component of global hydrological cycle,

371   the global mean precipitation has nearly no trend (Fig. 3). It is of interest that the global

372   mean SST exhibits a long-term variability with a period of 50-100 years in this

373   simulation. Possible mechanism and processes causing this variability will be discussed

374   in a follow-up study.

375     To further verify the stability of ocean component model, more variables are

376   represented in Fig. 4. At the beginning of the PI experiment (coupled model spin up), the

377   sea surface salinity (SSS) has a quick adjustment process. The global mean SSS is

378    decreased from 34.6 psu to 34.2 psu in 30 years. After the spin up, the mean value of SSS

379    is 34.2 psu, which is 0.5 psu fresher than the observed value. The long-term trend of SSS

380    is -0.0077 psu $(100yr)^{-1}$, which indicates the ocean water flux is maintained at a relatively

381    stable state. Meanwhile, the global mean sea water salinity (SWS) is 34.7 psu with a

382    linear trend of -0.0038 psu $(100yr)^{-1}$. The total sea water temperature has an increase

383    trend of 0.032 ℃ $(100yr)^{-1}$, this is consistent with the surface energy budget which shows

384    a 0.43 W $m^{-2}$ heating at the ocean surface. Furthermore, the linear trend at the last 100

385    year is smaller than the first 100 year. The decrease of linear trend implies the model

386    becomes more and more stable during the integration.

387    Atlantic Meridional Overturning Circulation (AMOC) is a major source of

388    decadal/multidecadal variability of the Earth system, and influences the Arctic sea ice

389    extent variability over Atlantic sector (Mahajan et al. 2011). The time series of the

390    maximum strength of the Atlantic Meridional Overturning Circulation (AMOC) at

391    26.5 °N is evaluated. The mean strength of AMOC is 14.8 sv, which is underestimated

392    comparingclose to the modern observational value of 18.5 sv (Cunningham et al.

393    2007) . ). The AMOC strength has a small linear trend and significant multidecadal

394    variability.

395    The middle and high latitude climate, as well as AMOC, is largely affected by sea ice

396    state and its variability. Following the IPCC report, the February, September and annual

397    mean of Northern and Southern Hemisphere sea ice extents (SIEs) are diagnosed for the

398    entire PI experiment period. The time evolutions of SIEs are plotted in Fig. 5. In the

399    Northern Hemisphere (NH), the annual mean, February and September mean SIE are 11

400    x $10^6$ $km^2$, 12.7x $10^6$ $km^2$, and 7.58x $10^6$ $km^2$, respectively. The trends of SIE over the

18

401 NH in the annual mean, February and September mean SIE are 0.039 x $10^6$ km$^2$(100yr)$^{-1}$,

402 0.06 x $10^6$ km$^2$(100yr)$^{-1}$, and 0.02x $10^6$ km$^2$(100yr)$^{-1}$, respectively. These trends are small,

403 suggesting that the Arctic SIE maintains a steady state. Over the SH, on the other hand,

404 the trends in the annual mean, February and September mean SIE are -0.07 x $10^6$km$^2$

405 (100yr)$^{-1}$, -0.002 x $10^6$ km$^2$ (100yr)$^{-1}$, and -0.1 x $10^6$ km$^2$(100yr)$^{-1}$, respectively. This

406 indicates that a significant trend exits in the SH September only. The annual mean,

407 February and September mean SIEs are 7.27 x $10^6$ km$^2$, 1.73x $10^6$ km$^2$, and 11.7x $10^6$

408 km$^2$, respectively, ~~indicating the SIEs are even less than recent decade's observation (e.g.,~~

409 ~~1980-2009).~~. The bias of the SH sea ice extent is related to the extensive solar radiation

410 over the Southern Ocean although the model overestimated cloud cover over there (figure

411 not shown). This is in part due to the thinner cloud optical depth in the simulated low-

412 level cloud and shallow mixed layer depth over the Southern Ocean (Sterl et al. 2012).

## 5. Simulated climatology

414     The climatological mean states of some key fields for energy and water balance

415 obtained from the average results for the last 100-year of the PI control run are compared

416 with observations, including TOA energy fluxes, ~~Outgoing Longwave Radiation (OLR),~~

417 SST, land surface temperature, precipitation, atmospheric zonal mean zonal wind,

418 temperature and specific humidity, and sea surface salinity. The observed ~~OLR~~ energy

419 fluxes data covers the period of 2001-2014 and the observed SST is averaged over the

420 period of 1870-1880. The observational estimate of the land surface temperature is based

421 on 1901-1910 mean of CRU-TS-v3.22. The rest of mean states are derived for the period

422 of 1979-2008.

423    The observed and simulated annual mean net shortwave (SW) radiation at the TOA

424    and the model bias are shown in Fig 6.  The simulated global mean net solar radiation is

425    238.65 W m$^{-2}$ which is smaller than the observation from CERES-EBAF data (Table 1).

426    The model bias indicates the excessive SW absorption over the ITCZ region and the

427    Southern Ocean, and less SW reflection over the middle latitude oceans that implies the

428    planetary albedo is too high.

429    Figure 6 7 shows the outgoing longwave radiation (OLR) which is balanced by the

430    TOA net downward solar radiation and represents the atmospheric and cloud top

431    temperature distribution. The global mean OLR is -238.45 W m$^{-2}$ in the model that is

432    close to the counterpart from the CERES data and the differences are within the range of

433    uncertainty among different observations (Loeb et al. 2009). The model simulates well

434    the vigorous deep convection-related low OLR over the Indo-Pacific warm pool as well

435    as the high OLR in the desert and subtropical regions. However, the model overestimates

436    the OLR over the majority of ITCZ, Indo-Pacific warm pool regions, and the off-South

437    American coast region in the South Pacific. The model also underestimates the OLR in

438    the North Atlantic storm track and western part of the Pacific subtropical high regions.

439    These biases arise primarily from the errors in simulated cloud fields.

440    The cloud radiative effect is defined as the difference between the clear-sky and full-

441    sky radiation. It indicates how cloud affects the radiation budget at the TOA. The

442    simulated SW and longwave (LW) cloud radiative effects (CRE) are compared with the

443    CERES-EBAF ed2.8 in Figure 8 and 9, respectively. The NESM v3 model simulates a

444    global averaged annual mean SW CRE of -48.4 W m$^{-2}$ compare to the observed value of -

445    47.2 W m$^{-2}$. The simulated LW CRE is 25.98 W m$^{-2}$ which is close to the observed value

20

446 of 25.75 W m$^{-2}$. The total cloud radiative effect in the NESM v3 is -22.5 W m$^{-2}$, this is

447 comparable with the CERES-EBAF observation (-21.45 W m$^{-2}$). The bias pattern of SW

448 CRE is similar to that of the net SW radiation at TOA. The model produces positive SW

449 CRE over the tropics although the simulated cloud cover bias is small (figure not shown).

450 This suggests the importance of cloud vertical distribution and cloud properties in

451 determining the CRE.  In addition, the LW CRE bias is smaller than the SW CRE

452 indicating the model has better representation of high cloud.

453  Figure 7 10 represents the simulated SST and its bias. SST is one of the most important

454 variables in the coupled system which reflects the quality of the model's simulation of

455 atmosphere-ocean interaction processes. The model well captures global distribution of

456 SST with a warm pool in the Indo-Pacific region and the cold tongue over the eastern

457 Pacific. There are warmer biases in the Southern Ocean and off the western coasts of

458 America and Africa, which link to the excessive downward shortwave radiation induced

459 by the negative bias in simulated stratiform clouds. Significant cold SST biases are found

460 in the high-latitude North Atlantic around 50 °N with a maximum negative bias of -4 K.

461 Cold biases are also seen in the subtropical North Pacific and North Atlantic.

462  The land surface temperatures (LST, Figure 11) are shown in comparison with CRU-

463 TS-v3.22 (1901-1910). The model well reproduces the basic patterns of the LST,

464 including warm continents in equatorial regions and cold continents close to Polar

465 Regions. The simulated global averaged (70 °S-90 °N) LST is 12.72 ℃, which is slightly

466 warmer than the observed value of 12.58 ℃ (Table 1). The warm temperature bias is

467 mainly found over Central Asian, Canadian and Australian Continent.

468    ——Figure 8 12 compares the spatial pattern of observed and simulated precipitation.

469    The simulated precipitation pattern and intensity resemble the observations (pattern

470    correlation coefficient, PCC=0.85), which capture the observed rain bands over ITCZ,

471    South Pacific Convergence Zone (SPCZ), tropical Indian Ocean and the midlatitude

472    storm track regions.  However, the so-called double-ITCZ precipitation bias exists in the

473    Pacific Ocean and Atlantic Ocean, which is likely partially linked to simulated TOA

474    shortwave radiation bias (Xiang et al. 2017) and the deficiency in deep convective

475    parameterization that results in insufficient stratocumulus clouds over eastern Pacific

476    (Bacmeister et al. 2006, Song and Zhang 2009). The precipitation bias shows a dipole

477    pattern over the tropical Indian Ocean. From an atmospheric point of view, such a model

478    deficiency is mainly attributed to the SST bias over the tropics, but it is essentially a

479    coupled model bias.

480      The zonal mean climatological temperature, zonal wind, and specific humidity along

481    with their biases with respect to ERA-interim, are presented in Fig. 13-15. Overall, the

482    model captures the temperature, zonal wind and specific humidity distribution reasonably

483    well. The temperature and zonal wind biases are small over majority of the region.

484    However, there exist 6-K cold biases at 200 hPa over high latitudes in both hemispheres

485    (Fig. 13). The biases increase the tropics-to-pole temperature gradient in the upper

486    troposphere, which produced an enhanced subtropical jet. The westerly wind bias is about

487    $6 \text{ m s}^{-1}$ in the subtropical jet of both hemispheres and over the equator in the upper-

488    troposphere (Fig. 14). The model simulated less water vapor within the boundary layer

489    while overestimated the specific humidity above the boundary layer (Fig. 15).

490    ——The sea surface salinity (SSS) is an integrated indicator for the hydrological

491    interaction among ocean, atmosphere, land runoff and sea ice, as well as ocean

492    circulation. Accurate simulation of ocean circulation in climate models is essential for

493    correct estimation of the transient ocean heat uptake and climate response, sea level rise,

494    and coupled modes of climate variability. Figure 16 shows the observed climatological

495    SSS and the model bias. In general, the model simulates realistically the high SSS over

496    the subtropics, where precipitation is low and evaporation is high, and the relatively low

497    SSS over the ITCZ region where precipitation is heavy. The global mean SSS has a

498    negative bias of 0.5 psu, which is mainly due to the fresh bias over the North Atlantic and

499    the western equatorial Pacific. Over the western equatorial Pacific, extensive

500    precipitation is the major cause. Over the North Atlantic, the excessive net input of fresh

501    water is a primary cause, which is augmented by weak evaporation at high latitudes. The

502    fresh water bias in the North Atlantic can also be attributed to the bias in simulated North

503    Atlantic Currents and excessive sea ice melt over the Labrador Sea. Previous studies

504    pointed out that the fresh water bias over high latitudes of North Atlantic can weaken

505    ocean convection, so that weaken the ~~Atlantic Meridional Overturning Circulation~~

506    ~~(AMOC)~~AMOC (Rahmstorf 1995).

507    The simulated February and September sea ice concentration in both hemispheres are

508    compared with observation in the period of 1870-1880 (Fig. 17, 18). In the NH, the

509    spatial distribution of summer and winter sea ice concentration is well captured by the

510    NESM v3.  Over the Southern Hemisphere, the model significantly underestimates sea

511    ice concentration, especially during austral summer. As discussed in the previous section,

512     there is an extensive solar radiation bias over the Southern Ocean which leads to the

513     warm SST bias, especially during local summer when solar radiation is high.

## 6. Climate sensitivity to $CO_2$ forcing

515     Quantification of climate response to different forcing and estimation of the associated

516     radiative forcing can be benefited from sensitive experiments with a single perturbation

517     forcing, such as an abruptly quadrupling $CO_2$ (abrupt-4xCO2) simulation and a 1% $yr^{-1}$

518     $CO_2$ increase (1pctCO2) experiments. Following the CMIP6 protocols, the two $CO_2$

519     experiments are designed to document basic aspects of the NESM v3 model response to

520     greenhouse gas forcing. They are both branched from the PI simulation and the only

521     difference are the imposed $CO_2$ concentrations. In the abrupt-4xCO2 experiment, the

522     atmospheric $CO_2$ concentration is abruptly quadrupled (1139 ppm) with respect to the PI

523     condition (274.75 ppm) in the very beginning of the experiment. The 1pctCO2 is

524     designed as gradually increasing the $CO_2$ concentration at the rate of 1% per year. Both

525     experiments were initiated at the end of year 100 of the PI experiments, and each of them

526     was integrated for 150 yrs.

527     Figure 19 shows the global annual mean surface air temperature (TAS) changes with

528     respect to its mean value in the PI experiment. Once the atmospheric $CO_2$ instantaneous

529     quadrupling, the radiative forcing defined by the net downward heat flux induced by the

530     changing atmospheric carbon dioxide concentration forces the stratospheric and

531     tropospheric circulations to adjust, thereby changing the surface temperature. The TAS

532     rapidly increases by approximately 4.5 K in the first 20 years in response to the imposed

533   radiative forcing. After the rapid initial increase, the TAS gradually increases, mitigating

534   the energy imbalance at the TOA.

535   The abrupt 4 x_CO$_2$ experiment is used not only to diagnose the fast response of the

536   Earth system, but also to quantify the radiative forcing, as well as to estimate the

537   Equilibrium Climate Sensitivity (ECS). The ECS is regarded as the global equilibrium

538   TAS change in response to the ~~quadrupling~~ doubling atmospheric carbon dioxide

539   concentration. It is also indicated by the ~~product~~ ratio of the radiative forcing ~~and~~ to the

540   climate feedback parameter. The regression of TOA energy imbalance and global mean

541   TAS change is an effective method to obtain those estimations (Gregory et al. 2004),

542   since~~. It~~ it doesn't require the equilibrium state of GCM. The intersection of regression

543   line and the y-axis is recognized as the adjusted radiative forcing, and the intersection on

544   the x-axis is an indication of the equilibrium temperature. The slope of the regression line

545   is the climate feedback parameter.

546   The relationship between the change in the net TOA energy imbalance and global

547   mean TAS change is plotted in Fig. 20~~11~~. ~~Figure 11~~It shows that the TOA radiative

548   imbalance is around 7.24 W m$^{-2}$ when the assumed global TAS is unchanged, although

549   the radiative forcing is affected by the rapid adjustments of stratosphere in the first year

550   and therefore reduced the effective radiative forcing (Gregory and Webb 2008). To

551   balance the net TOA energy, the regression predicted an equilibrium temperature change

552   of 7.38 K in this model, yields a climate feedback parameter of -0.98_Wm$^{-2}$K$^{-1}$. Since the

553   radiative forcing is logarithmically related to the carbon dioxide concentration if we

554   approximate the climate feedback parameter as a constant ~~and the climate feedback~~

555   ~~parameter is considered as a constant in a giving model, even in the presence of other~~

25

556  forcing agents (Hansen et al. 2005), this gives the ECS of 3.69_K. Andrews et al. (2012)

557  found that the CMIP5 ensemble mean of regressed 4_x_$CO_2$ adjusted forcing is 6.89±1.12

558  W m$^{-2}$, and the climate feedback parameter is -1.08±0.29_Wm$^{-2}$K$^{-1}$, with the ECS of

559  3.37±0.29_K. The carbon dioxide-induced radiative forcing and climate feedback

560  parameter estimated by the NESM v3 model are comparable with CMIP5 model

561  ensemble, albeit the estimated ECS is about 10% higher.

562  The climate sensitivity parameter consists of the longwave clear sky, shortwave clear

563  sky, longwave cloud forcing and shortwave cloud forcing terms. They are defined by the

564  heat flux differences between the abrupt-4xCO2 experiment and PI experiment. The sum

565  of the longwave cloud forcing and shortwave cloud forcing is the total CRE. Here the

566  downward fluxes are defined as positive. Figure 21̶1̶2̶ shows the relationships between

567  the changes in the global mean heat fluxes and the change in the surface air temperature.

568  The longwave clear sky feedback strenghth is -1.63_Wm$^{-2}$K$^{-1}$, which is partially offset by

569  the shortwave clear sky feedback (0.68_Wm$^{-2}$K$^{-1}$), resulting in a residual feedback

570  strength of -0.95_Wm$^{-2}$K$^{-1}$, which is close to the climate sensitivity parameter estimated in

571  this model (-0.98_Wm$^{-2}$K$^{-1}$). The slopes of the shortwave and longwave cloud forcing

572  have nearly the same magnitude but with opposite signs, yielding a small positive cloud

573  radiative effect (0.02_Wm$^{-2}$K$^{-1}$) in this model. It could be the reason of slightly high ECS

574  of NESM v3 since the CMIP5 model results suggested that ̶T̶h̶e̶ ̶r̶e̶s̶u̶l̶t̶ ̶h̶e̶r̶e̶ ̶i̶s̶ ̶c̶o̶n̶s̶i̶s̶t̶e̶n̶t̶

575  ̶w̶i̶t̶h̶ ̶t̶h̶e̶ ̶c̶o̶n̶c̶l̶u̶s̶i̶o̶n̶ ̶d̶e̶r̶i̶v̶e̶d̶ ̶f̶r̶o̶m̶ ̶t̶h̶e̶ ̶a̶n̶a̶l̶y̶s̶i̶s̶ ̶o̶f̶ ̶t̶h̶e̶ ̶C̶M̶I̶P̶5̶ ̶m̶o̶d̶e̶l̶s̶,̶ ̶t̶h̶a̶t̶ ̶i̶s̶,̶ ̶a̶ the GCM

576  with higher sensitivity is associated with a positive CRE feedback (Andrews et al. 2012).

577  And the̶T̶h̶e̶ CRE is a major contributor to the uncertainty in climate sensitivity parameter

578  in CMIP3 and CMIP5 models, although its magnitude is small compared to other flux

579  terms (Webb et al. 2006, Andrews et al. 2012).

580  Figure 22~~13~~ displays the global distributions of temperature and precipitation in

581  response to the quadrupling $CO_2$ forcing, which are defined by the departure of the last

582  30-year climatology from the corresponding climatology in the PI experiment. The most

583  pronounced warming is seen over the Arctic region where sea ice albedo feedback

584  dominates (Screen and Simmonds 2010). The relative small temperature change is over

585  the Southern Ocean and North Atlantic. The warming is more significant over land than

586  ocean, especially in the Northern Hemisphere. The mean surface temperature over land

587  and ocean are 8.0 K and 5.2 K, respectively. The equatorial Pacific shows an El Nino-like

588  warming. The zonal mean surface temperature change shows an obvious polar

589  amplification, especially over the Arctic Ocean; and stronger warming over the NH high

590  latitudes and weak warming in the SH middle latitudes. The Large NH temperature

591  increase is attributed to the strong warming over the Arctic Ocean and the large land area

592  in the NH.

593  A direct consequence of global warming is the rising atmospheric specific humidity

594  and precipitation. The global mean precipitation is increased from 2.87 mm day$^{-1}$ to 3.12

595  mm day$^{-1}$, resulting in a precipitation increase of 1.4% per Kelvin global warming.

596  Significant precipitation increases are seen in the equatorial Pacific and Northern Indian

597  Ocean as well as along the Pacific storm track (Fig. 22~~13~~). Decreased precipitation is

598  evident in the sub-tropical descent zones. Note that precipitation is decreased over the

599  Amazon region, where the model has a dry bias in climatology. The global distribution of

600     precipitation change appears to be dominated by the wet-get-wetter ~~(Held and Soden,~~

601     ~~2006)~~ pattern (Held and Soden, 2006).

602     In reality, the $CO_2$ increase is gradually rather than abrupt. The 1pctCO2 experiment is

603     designed to examine the transient climate response (TCR), which is calculated by using

604     the global mean TAS change between the averaged 20-year period centered at the timing

605     of $CO_2$ doubling (year 60-80 in 1pctCO2 experiment) and the PI experiment. The time

606     evolution of the global mean TAS anomalies with respect to the PI experiment is shown

607     in Fig. 23~~14~~. A linear increase of temperature anomalies is presented in the gradually

608     $CO_2$ increasing experiment. The temperature anomalies averaged between year 60 and 80

609     are 2.16 K. This value of TCR is significantly small than the ECS, demonstrating that the

610     ocean heat uptake delays surface warming. The estimation from CMIP5 models shows

611     that the mean TCR is 1.8±0.6 K (Flato et al. 2013), implying that the NESM v3 is

612     comparable to other CGCMs.

613 **6. Conclusion**

614     The development of version 3 of the Nanjing University of Information Science and

615     Technology (NUIST) Earth System Model (NESM v3) aims at building up a

616     comprehensive numerical modeling laboratory for multi-disciplinary studies of the

617     Climate System and Earth System. As a subsequent version of NESM v1, it has upgraded

618     the atmospheric and land surface models, increased the ocean model resolution, improved

619     coupling conservation and modified model physics.

620     The NESM v3 couples the ECHAM v6.3 atmospheric model, JSBACH land surface

621     model, NEMO v3.4 ocean model, and CICE v4.1 sea ice model by using OASIS3-

622  MCT_3.0 coupler. The improvement of model physics mainly focuses on convective

623  parameterizations, cloud macrophysics and microphysics, and ocean-sea ice coupling.

624  The model physics modifications and parameters adjustments are targeted at (1)

625  obtaining stable long-term integrations and reasonable global mean states under the

626  preindustrial (PI) forcing, (2) mitigating the biases in the mean climatology and internal

627  modes of climate variability with respect to the modern observations in the present-day

628  forcing condition, and (3) simulating reasonable climate responses to transient and abrupt

629  $CO_2$ forcing.

630  A 500-yr PI experiment is conducted and analyzed to test the model's computational

631  stability. As shown in Sec. 4, the long-term climate drifts in NESM v3 are generally

632  negligibly small, especially in the global radiative energy and temperature. The simulated

633  net downward energy flux at the TOA and surface are 0.17 $Wm^{-2}$ and 0.35_$Wm^{-2}$,

634  respectively. The near-equilibrium model long-term temperature evolution is benefited

635  from the near-zero energy imbalance and negligibly small trends in the energy balance.

636  The global mean near surface air temperature is 14.92℃ with a trend of ~~0.0096~~0.00214 ℃

637  $(100yr)^{-1}$. The linear trends of the land surface and sea surface temperature are -

638  ~~0.016~~0.00984℃ $(100yr)^{-1}$ and ~~0.0026~~0.00731℃ $(100yr)^{-1}$, respectively. However, the

639  total sea water temperature has a warming trend of 0.03℃ $(100yr)^{-1}$, which can be

640  explained by the small but persistent positive downward energy flux into the ocean. The

641  stable long-term evolutions of precipitation, sea surface salinity (SSS) and sea water

642  salinity (SWS) demonstrate the conservation of global water. At the beginning of PI

643  experiments spin up, there was a freshening trend in SSS, which is associated with the

644  ocean adjustment. The fresher SSS has no significant influence on ~~SWT~~SWS. After the

645 spin up, the global mean SSS and ~~SWT~~ SWS have no appreciable trends although the

646 SSS is fresher than the observed counterpart. The Northern Hemispheric annual mean,

647 February, and September mean SIEs maintain a steady value at 11.4 x $10^6$ km$^2$, 13.4x $10^6$

648 km$^2$, and 7.78x $10^6$ km$^2$, respectively. However, the simulated Southern Hemisphere SIEs

649 are less than present-day observation. The conservation properties of NESM v3 are

650 encouraging, fulfilling a highly desirable constraint for climate models aiming for

651 multidecadal, centennial and longer simulations.

652 The last 100-year results are compared with the available observations as presented in

653 Table 1. The TOA energy budget and cloud radiative effect are attracted more attention

654 since its importance in understanding the climate change. The model results show a

655 realistic global climate, although the bias of energy state still exists, especially over Indo-

656 Pacific region, which may be related to the treatment of cloud and convection

657 parameterization. The ~~The model simulates realistic OLR pattern, although it~~

658 ~~overestimates OLR over the ITCZ and Indo-Pacific warm pool regions as well as off the~~

659 ~~South American coast in the South Pacific whereas underestimates the OLR in the North~~

660 ~~Atlantic storm track and western Pacific subtropical high regions. The~~ annual mean

661 SST/LST is well produced in the model, but large cold biases exist in the North Atlantic

662 and significant warm biases in the Southern Ocean, and warm temperature bias over the

663 central Asian. ~~The biases in OLR and SST are primarily associated with the errors in the~~

664 ~~simulated cloud fields except for the North Atlantic cold bias.~~ The simulated mean

665 precipitation is reasonably realistic, but ~~slightly~~ suffers the double ITCZ syndrome. The

666 fresh bias in SSS in the tropical western North Pacific can be attributed to the extensive

667 precipitation and the fresh bias over the mid-latitude North Atlantic is related to

668 underestimated evaporation. The sea ice coverage is well reproduced by the model over

669 the Arctic in February and September; however, it is underestimated over the Antarctic

670 where SST has a warm bias.

671    The model produces a radiative forcing, under the abrupt quadrupling carbon dioxide,

672 of 7.24 W m$^{-2}$ with a climate feedback parameter of -0.98 Wm$^{-2}$K$^{-1}$, yielding a warming

673 of 7.38 K at the estimated equilibrium state. The transient climate sensitivity is 2.16 K

674 which is estimated from the 1% yr$^{-1}$ CO$_2$ gradually increasing experiment. The NESM v3

675 model is amongst the more sensitive side of the CMIP5 class of global climate models.

676    At last, this paper isn't aimed at providing a comprehensive evaluation of all model

677 aspect. The NESM v3 model'Its response to given SST forcing in AMIP and the

678 historical forcing in the coupled model, and the corresponding modern climatology,

679 internal and coupled modes of climate variability, as well as regional climate variability

680 will be discussed in detail in an accompanying paper later.

681

682    Code availability

683    Please contact Jian Cao (Email: jianc@nuist.edu.cn) to obtain the source code and data

684 of NESM v3.

685

692

693    **Reference**

694    Adcroft, A., Hill, C., Marshall, J.: Representation of topography by shaved cells in a

695         height coordinate ocean model. Mon. Weather Rev., 125, 2293-2315, 1997.

696    Andrews, T., Gregory, J. M., Webb, M. J., Taylor, K. E.: Forcing, feedbacks and climate

697         sensitivity in CMIP5 coupled atmosphere-ocean climate models. Geophysical

698         Research Letters, 39(9), 2012.

699    Bacmeister, J. T., Suarez, M. J., and Robertson, F. R.: Rain reevaporation, boundary

700         layer–convection interactions, and Pacific rainfall patterns in an AGCM. J. Atmos.

701         Sci., 63, 3383–3403, 2006.

702    Barnier, B., G. Madec, T. Penduff, J.-M. Molines, A.-M. Treguier, J. L. Sommer, A.

703         Beckmann, A. Biastoch, C. Boning, J. Dengg, C. Derval, E. Durand, S. Gulev, E.

704         Remy, C. Talandier, S. Theetten, M. Maltrud, J. McClean, and CuevasB. D.:

705         Impact of partial steps and momentum advection schemes in a global ocean

706         circulation model at eddy-permitting resolution. Ocean Dyn., 56, 543–567. 2006.

707    Bernard, B., Madec, G., Penduff ,T., et al: Impact of partial steps and momentum

708         advection schemes in a global ocean circulation model at eddy-permitting

709         resolution. Ocean Dyn., 56, 543-567, 2006.

710 Brinkop, S. and Roeckner, E.: Sensitivity of a general circulation model to
711     parameterizations of cloud-turbulence interactions in the atmospheric boundary layer.
712     Tellus, 47A,197–220, 1995.

713 Brovkin, V., Boysen, L., Raddatz,T., Gayler,V., Loew,A., and Claussen , M. :Evaluation
714     of vegetation cover and landsurface albedo in MPI-ESM CMIP5 simulations, J.
715     Adv. Model. Earth Syst., 5, 48–57, doi:10.1029/2012MS000169, 2013.

716 Cao, J., and Wu, L.: Asymmetric impact of last glacial maximum ice sheets on global
717     monsoon activity. Journal of the Meteorological Sciences, 36(4):425-435,2016.

718 Cao, J., Wang, B., Xiang, B., Li, J., Wu, T., Fu, X., Wu, L. Min, J.: Major modes of
719     short-term climate variability in the newly developed NUIST Earth System Model
720     (NESM). Adv. Atmos. Sci., 32(5), 585–600, doi: 10.1007/s00376-014-4200-6,
721     2015.

722 Cunningham, S. A., Kanzow, T., Rayner, D., Baringer, M. O., Johns, W. E., Marotzke, J.,
723     Longworth, H. R., Grant, E. M., Hirschi, J. J.-M., Beal, L. M., Meinen, C.S.,
724     Bryden, H. L.: Temporal variability of the Atlantic Meridional Overturning
725     Circulation at 26°N. Science, 317, 935-938, 2006.

726 Dee, D. P., Uppala, S. M., Simmons, A. J., Berrisford, P., Poli, P., Kobayashi, S., Andrae,
727     U., Balmaseda, M. A., Balsamo, G., Bauer, P., Bechtold, P., A. Beljaars, C. M., van
728     de Berg, L., Bidlot, J., Bormann, N., Delsol, C., Dragani, R., Fuentes, M., Geer, A.
729     J., Haimberger, L., Healy, S. B., Hersbach, H., Hólm, E. V., Isaksen, L., Kållberg,
730     P., Köhler, M., Matricardi, M., McNally, A. P., Monge-Sanz, B. M., Morcrette, J.-
731     J., Park, B.-K., Peubey, C., de Rosnay, P., Tavolato, C., Thépaut, J.-N., and Vitart,
732     F.:The ERA-Interim reanalysis: configuration and performance of the data

733        assimilation system, Q. J. R. Meteorol. Soc., 137,553 597. doi: 10.1002/qj.828,

734        2011.

735    Eyring, V., Bony, S., Meehl, G. A., Senior, C. A., Stevens, B., Stouffer, R. J., and Taylor,

736        K. E.: Overview of the Coupled Model Intercomparison Project Phase 6 (CMIP6)

737        experimental design and organization, Geosci. Model Dev., 9, 1937-1958,

738        doi:10.5194/gmd-9-1937-2016, 2016.

739    Flato, G., Marotzke, J., Abiodun, B., Braconnot, P., Chou, S. C., Collins, W., Cox, P.,

740        Driouech, F., Emori, S., Eyring, V., Forest, C., Gleckler, P., Guilyardi, E., Jakob,

741        C., Kattsov, V., Reason, C., and Rummukainen, M.: Evaluation of Climate Models,

742        in: Climate Change 2013: The Physical Science Basis, Contribution of Working

743        Group I to the Fifth Assessment Report of the Intergovernmental Panel on Climate

744        Change, edited by: Stocker, T. F., Qin, D., Plattner, G.-K., Tignor, M., Allen, S. K.,

745        Boschung, J., Nauels, A., Xia, Y., Bex, V., and Midgley, P. M., Cambridge

746        University Press, Cambridge, United Kingdom and New York, NY,USA, 2013.

747    Fu, X., and Wang, B.: Critical roles of the stratiform rainfall in sustaining the Madden-

748        Julian Oscillation: GCM Experiments. J. Climate, 22 (14) 3939–3959, 2009.

749    Gent, P. R. and McWilliams, J. C.: Isopycnal mixing in ocean circulation models. J. Phys.

750        Oceanogr., 20, 150-155, 1990.

751    Giorgetta, M. A., Roeckner, E. Mauritsen, T., Bader, J., Crueger, T., Esch, M., Rast, S.,

752        Kornblueh, L., Schmidt, H., Kinne, S. Hohenegger, C. Möbis, B. Krismer, T.,

753        Wieners, K.–H. Stevens, B.: The Atmospheric General Circulation Model

754        ECHAM6: Model Description, Tech. rep., Max Planck Institute for Meteorology,

755        Hamburg, Germany. 2013.

756    Gregory, J. M., and Webb, M. J.: Tropospheric adjustment induces a cloud component in

757        CO2 forcing, J. Clim., 21, 58–71, doi:10.1175/2007JCLI1834.1, 2008.

758    Gregory, J. M., Ingram, W. J., Palmer, M. A., Jones, G. S. Stott, P. A. Thorpe, R. B.

759        Lowe, J. A., Johns, T . C., and Williams, K. D.,: A new method for diagnosing

760        radiative forcing and climate sensitivity, Geophys. Res. Lett., 31, L03205,

761        doi:10.1029/2003GL018747, 2004.

762    Ham, Y.-G., Kug, J.-S.: ENSO phase-locking to the boreal winter in CMIP3 and CMIP5

763        models. Clim Dyn 43:305–318.doi:10.1007/s00382-014-2064-1,2014.

764    Hansen, J., et al. Efficacy of climate forcings, J. Geophys. Res., 110, D18104,

765        doi:10.1029/2005JD005776, 2005.

766    Hansen, J., Nazarenko, L., Ruedy, R., Sato, M., Willis, J., DelGenio, A., Koch, D., Lacis,

767        A., Lo,K.,Menon, S., Novakov, T., Perlwitz, J., Russell, G., Schmidt, G.A.,

768        and Tausnev, N.: Earth's energy imbalance: Confirmation and

769        implications. *Science*, 308, 1431-1435, doi:10.1126/science.1110252, 2005.

770    Harris, I., Jones, P., Osborn, T., and Lister, D.: Updated high-resolution grids of monthly

771        climatic observations - the CRU TS3.10 dataset, International Journal of

772        Climatology, 34, 623–642, 2014.

794    Held, I. M., and Soden, B. J.: Robust response of the hydrological cycle to global

795        warming, J. Clim., 19, 5686 – 5699, 2006.

796    Hourdin, F., Mauritsen, T., Gettelman, A., Golaz, J.-C., Balaji, V., Duan, Q., Folini, D., Ji,

797        D., Klocke, D., Qian, Y., Rauser, F., Rio, C., Tomassini, L., Watanabe, M., and

798        Williamson, D.: The art and science of climate model tuning. Bulletin of the

799        American Meteorological Society 98, 589–602, doi:10.1175/bams-d-15-00135.1,

800    2017.

801    Hunke, E. C.: Thickness sensitivities in the CICE sea ice model. Ocean Modelling, 34,pp.

802        137-149. doi:10.1016/j.ocemod.2010.05.004. LA-UR-10-00585, 2010.

803    Hunke, E. C, and Dukowicz, J. K.: The elastic–viscous–plastic sea ice dynamics model in

804        general orthogonal curvilinear coordi- nates on a sphere—Incorporation of metric

805        terms. Mon. Wea. Rev., 130, 1848–1865, 2002.

806    Hunke, E. C., and Lipscomb, W. H.:CICE: The Los Alamos Sea Ice Model

807        Documentation and Software User's Manual Version 4.1. LA-CC-06-012, T-3

808        Fluid Dynamics Group, Los Alamos National Laboratory, Los Alamos N.M, 2010.

809    Iacono, M. et al.: Radiative forcing by long-lived greenhouse gases: Calculations with the

810        AER radiative transfer models. *J. Geophys. Res.*, 113, 2008.

811    Lee, J. Y., and Wang, B.: Future change of global monsoon in the CMIP5. Climate

812        Dynamics, 42, 101-119, 2014.

813    Lengaigne, M., Madec, G. Bopp, L. Menkes, C. Aumont, O. and Cadule, P.: Bio-physical

814        feedbacks in the Arctic Ocean using an Earth system model. Geophys. Res. Lett.,

815        36, L21602. doi: 10.1029/2009GL040145, 2009.

816    Li, J., Wang, B., and Yang, Y.M.: Retrospective seasonal prediction of summer monsoon

817        rainfall over West Central and Peninsular India in the past 142 years. Climate Dyn.,

818        48(7), 2581-2596, 2017.

819    Locarnini, R. A., Mishonov, A. V., Antonov,J. I., Boyer, T. P., Garcia, H. E., Baranova,

820        O. K., Zweng, M. M., and Johnson, D. R. World Ocean Atlas 2009, Volume 1:

821        Temperature. S. Levitus, Ed. NOAA Atlas NESDIS 68, U.S. Government Printing

822        Office, Washington, D.C., 184 pp, 2010.

Loeb, N. G., Wielicki, B. A., Doelling, D. R., Smith, G. L., Keyes, D. F.; Kato, S., Manalo-Smith, N., Wong, T.: Toward Optimal Closure of the Earth's Top-of-Atmosphere Radiation Budget Journal of Climate, 22(3), 748-766. http://dx.doi.org/10.1175/2008JCLI2637.1, 2009.

Lott, F.: Alleviation of Stationary Biases in a GCM through a Mountain Drag Parameterization Scheme and a Simple Representation of Mountain Lift Forces. Mon Weather Rev, 127 (5), 788-801, 1999.

Lott, F. and Miller, M. J.: A new-subgrid-scale orographic drag parameterization: Its formulation and testing. Quart. J. Roy. Meteor. Soc., 123, 101–127, 1997.

Luo, X. Wang, B.: Predictability and prediction of the total number of winter extremely cold days over China. Clim. Dyn. 50, 1769-1784, 2018.

Lumpkin, R., and Speer, K.: Global ocean meridional overturning. J. Phys. Oceanogr., 37, 2550–2562, 2007.

Madec, G. and Imbard M. : A global ocean mesh to overcome the North Pole singularity. Climate Dynamics, 12, 381-388,1996.

Mahajan., S., Zhang, R., Delworth, T. L.: Impact of the Atlantic Meridional Overturning circulation (AMOC) on Arctic surface air temperature and sea ice variability. Journal of Climate, 24, 6573-81, 2011.

Meehl, G. A., Boer, G.J., Covey, C. Latif, M. and Stouffer, R. J.: The Coupled Model Intercomparison Project (CMIP). Bull. Amer. Metero. Soc., 81, 313-318, 2000.

Miller, M. J., T. N. Palmer, and R. Swinbank: Parametrization and influence of subgridscale orography in general circulation and numerical weather prediction models. Meteorl. Atmos. Phys., 40 (1), 84-109, 1989.

846     Nordeng, T. E.: Extended versions of the convective parameterization scheme at

847          ECMWF and their impact on the mean and transient activity of the model in the

848          tropics. Tech. Rep. 206, ECMWF, Reading, 1994.

849     Raddatz, T. J., Reick, C.H., Knorr, W., Kattge, J., Roeckner, E., Schnur, R., Schnitzler,

850          K.-G., Wetzel, P., Jungclaus, J.: Will the tropical land biosphere dominate the

851          climate-carbon cycle feedback during the twenty-first century? Clim. Dyn., 29,

852          565–574, 2007.

853     Rahmstorf, S. Bifurcations of the Atlantic thermohaline circulation in response to

854          changes in the hydrological cycle. *Nature*, 378(9), 145-149,1995.

855     Rayner, N. A., Parker, D. E.,Horton, E. B., Folland, C. K., Alexander, L. V., Rowell, D.

856          P., Kent, E. C., and Kaplan, A.: Global analyses of sea surface temperature, sea ice,

857          and nightmarine air temperature since the late nineteenth century. J. Geophys. Res.,

858          108, 4407, doi:10.1029/2002JD002670, 2003.

859     Redi, M. H.: Oceanic isopycnal mixing by coordinate rotation, J. Phys. Oceanogr., 12,

860          1154-1158, 1982.

861     Rothrock, D. A.: The energetics of the plastic deformation of pack ice by ridging. J.

862          Geophys. Res., 80, 4514–4519, 1975.

863     Roullet, G. and Madec, G.: Salt conservation, free surface and varying volume: A new

864          formulation for ocean GCMs. J. Geophys. Res., 105, 23927-23942, 2000.

865     Screen, J.A., Simmonds, I.: The central role of diminishing sea ice in recent Arctic

866          temperature amplification. Nature 464. doi:10.1038/nature0905, 2010.

867     Schmidt, G. A., Bader, D., Donner, L. J., Elsaesser, G.S., Golza, J.-C., Hannay, C.,

868          Molod, A., Neale, R., Saha, S.: Practice and philosophy of climate model tuning

869    across six U.S. modeling centers. Geosci. Model Dev. Discss., doi:10.5194/gmd-
870        2017-30, 2017.

871    Simmons, A. J. and Burridge, D. M.: An energy and angular-momentum conserving
872        vertical finite difference scheme and hybrid vertical coordinates. Mon. Wea. Rev.,
873        109,758–766, 1981.

874    Song, X., and Zhang, G.: Convection parameterization, tropical Pacific double ITCZ, and
875        upper-ocean biases in the NCAR CCSM3. Part I: Climatology and atmospheric
876        feedback. J. Climate, 22, 4299–4315, 2009.

877    Sterl., A., Bintanja, R., Brodean, L., Gleeson, E., Koenigk, T., Schmith, T., Semmler, T.,
878        Severijns, C., Wyser, K., Yang, S.: A look at the ocean in the EC-Earth  climate
879        model. Climate Dynamics 29:2631-2657, 2012.

880    Stevens, B., et al., 2012: The atmospheric component of the MPI-M Earth System Model:
881        ECHAM6. J. Adv. Model. Earth Syst., doi:10.1002/jame.20015.

882    Sundqvist, H., Berge, E. and Kristjansson, J. :Condensation and cloud parameterization
883        studies with a mesoscale numerical weather prediction model. Mon. Wea. Rev., 117,
884        1641–1657, 1989.

885    Tiedtke, M.: A Comprehensive Mass Flux Scheme for Cumulus Parameterization in
886        Large-Scale Models. Mon Weather Rev, 117 (8), 1779-1800, 1989.

887    Urrego-Blanco, J. R., N. M. Urban, E. C. Hunke, A. K. Turner, and N. Jeffery,
888        Uncertainty quantification and global sensitivity analysis of the Los Alamos sea ice
889        model, J. Geophys. Res. Oceans, 121, 2709–2732, doi:10.1002/2015JC011558,
890        2016.

891    Valcke, S., and Coquart, L.: OASIS3-MCT User Guide, OASIS3-MCT 3.0. CERFACS

892      Technical Report, CERFACS TR/CMGC/15/38, Toulouse, France., available at:

893      http://www.cerfacs.fr/oa4web/oasis3mct_3.0/oasis3mct_UserGuide.pdf, 2015.

894  Wengel, C., Latif, M., Park,W., Harlaß, J., Bayr, T.: Seasonal ENSO phase locking in the

895      Kiel Climate Model: The importance of the equatorial cold sea surface temperature

896      bias. Clim Dyn. DOI 10.1007/s00382-017-3648-3, 20187.

897  Xiang, B., Zhao, M., Held, I. M. & Golaz, J.-C. Predicting the severity of spurious

898     'double ITCZ' problem in CMIP5 coupled models from AMIP simulations. Geophys.

899     Res. Lett. 44, 1520–1527, 2017.

900  Xie, P., and Arkin, P.A.: Global precipitation: A 17-year monthly analysis based on

901      gauge observations, satellite estimates, and numerical model outputs. Bull. Amer.

902      Meteor. Soc., 78, 2539 – 2558, 1997.

903  Zalesak, S. T.: Fully multidimensional flux corrected transport algorithms for fluids. J.

904      Comput. Phys., 31, 335–362, 1979.

905  Zdunkowski, W. G., Welch, R. M. and Korb, G. J. : An investigation of the structure of

906     typical two-stream methods for the calculation of solar fluxes and heating rates in

907     clouds. Beitr. Phys. Atmos., 53, 147–166, 1980.

908

909

910

911

912

913

914

915

916

917

918

919

920

921

922

923

924

925

926

927

Table 1 Summery of the global averaged annual mean values for radiation, temperature and precipitation compare to observations. The observed energy estimations are from CERES ed2.8 on the period of 2001-2014. The observed SST/LST data is derived from Hadley SST/CUR on the period of 1870-1880/1901-1910. The combined CMAP and GPCP precipitation.

Figure1.Coupled structure of NESM v3 model.

Figure 2 Radiative energy balances in NESM v3. Time series of the net radiative energy fluxes at TOA (downward, W m$^{-2}$ upper) and the net heat flux at the Earth surface (W m$^{-2}$, bottom) from year 0 to year 500 in the Preindustrial control experiment. The long-term mean value and trend are indicated in the left upper corner. The black lines indicate annual mean values and the red lines indicate their 9-yr running mean values.

938    Figure 3 Results from the Preindustrial control experiment. Annual mean time series of the

939    surface temperature and precipitation from year 0 to year 500 in the Preindustrial control

940    experiment, from top, near surface air temperature (℃), land surface temperature (℃), sea surface

941    temperature (℃), and precipitation (mm d$^{-1}$). The long-term mean value and trend are indicated in

942    the left upper corners. The black lines are annual mean values and the red lines are their 9-yr

943    running mean values.

944    Figure 4 Results from the Preindustrial control experiment. Annual mean time series of the ocean

945    variables from year 0 to year 500 from top, sea surface salinity (psu); sea water salinity (psu); sea

946    water temperature (℃ ), AMOC strength at 26.5°N (sv). The sea water salinity and sea water

947    temperature are the volume-mean values for the full-depth global ocean. The long-term mean

948    value and trend are indicated in the left upper corner. The black lines are annual mean values and

949    the red lines are their 9-yr running mean values.

950    Figure 5 Results from the Preindustrial control experiment. The Northern Hemisphere (NH) and

951    Southern Hemisphere (SH) sea ice extents (SIEs, unit: $10^6$km$^2$) time series year 0 to year 500 in

952    the Preindustrial control experiment. The black, blue and green lines represent the annual mean,

953    February and September SIEs, and the red lines are the corresponding 9-yr running mean. The

954    long-term trends of annual mean SIEs are indicated in the left upper corner of each panel.

955    Figure 6  Annual mean  TOA net shortwave radiation ( units: W m$^{-2}$) derived from observation

956    (top), the model simulation in the PI experiment (middle) and the model bias (bottom). The

957    observed radiation~~feild~~field was derived from the Clouds and the Earth's Radiant Energy System

958    (CERES) dataset (Loeb et al. 2009).

959    Figure 7 As in Fig. 6 except for OLR.

960    Figure 8 As in Fig. 6 except for TOA shortwave cloud effect.

961    Figure 9 As in Fig. 6 except for TOA longwave cloud effect.

962 Figure 11 As in Fig. 10 except ~~The same as Figure 10, but~~ for land surface temperature (℃). The

963 observed land ~~surface climatology~~ surface climatology was derived from the CRU-TS-v3.22

964 (Harris et al. 2014) for the period of 1901-1910.


965 Figure 11 As in Fig. 10 except for land surface temperature (℃). The observed land surface

966 climatology was derived from the Hadley Center sea-Ice and Sea Surface Temperature (HadISST,

967 Rayner et al., 2003) for the period of 1870-1880.

968 Figure 12 The same as in Fig. 6 except for annual mean of precipitation (mm day$^{-1}$). The observed

969 precipitation was derived from a Merged precipitation dataset (Lee and Wang 2014), which is the

970 arithmetic mean of the monthly data from the Global Precipitation Climatology Project (GPCP)

971 version 2.2 (Adler et al., 2003) and Climate Prediction Center Merged Analysis of Precipitation

972 (CMAP, Xie and Arkin, 1997).

973 Figure 13 The zonal mean climatological of temperature in NESM v3, ERA-interim (1979-2008)

974 and model bias.

975 Figure 14 As in Fig. 13 except for zonal wind.

976 Figure 15 As in Fig. 13 except for specific humidity.

977 Figure 16 Same as in Fig. 6 except for the annual mean sea surface salinity (psu). The observed

978 SSS data are from the World Ocean Atlas 2009 (WOA09) (Locarnini et al. 2010).

979 Figure 17 Climatological Arctic sea ice concentration in NESM v3 (upper), HadISST (middle),

980 and model bias (bottom) for February (a,c,e) and September(b,d,f). The observed sea ice

981 concentration is averaged over the period of 1870-1880.

982 Figure 18 As in Fig. 17 except for Antarctic.

983 Figure 19 Results from the abrupt quadrupling $CO_2$ experiment. Global-mean surface air

984 temperature change relative to the counterpart in the PI experiment.

985 Figure 20 Results from the abrupt quadrupling $CO_2$ experiment. The relationships between the

986 change in the net TOA radiative flux and the global-mean surface air temperature in NESM v3

model. The solid line represents linear least squares regression fit to the 150 years of model output data. The interception at $\delta T = 0$ indicates the adjusted radiative forcing (F=7.24Wm$^{-2}$). The slope of the regression line measures the strength of the feedbacks in the climate system, the climate feedback parameter (-0.981 Wm$^{-2}$K$^{-1}$). The interception at x-axis gives the equilibrium $\delta T$ (7.38 K).

Figure 21 Results from the abrupt quadrupling $CO_2$ experiment. The relationship between the change in the global mean radiative fluxes and global mean surface air temperature change. The climate feedback parameters (Wm$^{-2}$ K$^{-1}$) for the TOA longwave clear sky (red), shortwave clear sky(green), longwave cloud forcing (blue), shortwave cloud forcing (light blue) and net cloud radiative effect (black) are -1.63, 0.675, 0.31, -0.30, 0.02 Wm$^{-2}$ K$^{-1}$, respectively.

Figure 22 Changes in the surface temperature (top) and precipitation (bottom) derived from the last 30-year climatology in the 150-year abrupt 4 x $CO_2$ experiments. The changes are with reference to the corresponding climatological mean fields from the PI experiment. The right panels show the corresponding zonal mean chnages.

Figure 23 Results from the 1%per year $CO_2$ increases experiment. Global mean annual surface air temperature change relative to counterpart in the PI experiment. The average temperature anomalies between year 60-80 is defined as transit climate sensitivity, which is 2.16 K in the NESM v3 model.

1012  0 to year 500 in the Preindustrial control experiment. The long term mean value and trend are

1013  indicated in the left upper corner. The black lines indicate annual mean values and the red lines

1014  indicate their 9-yr running mean values.

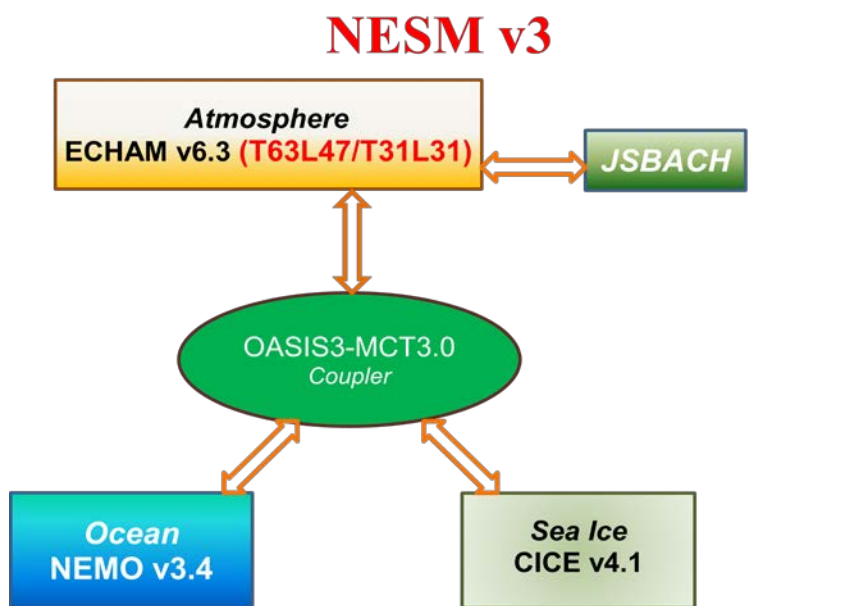1015  Fig. 3. Results from the Preindustrial control experiment. Annual mean time series of the surface

1016  temperature and precipitation from year 0 to year 500 in the Preindustrial control experiment,

1017  from top, near surface air temperature (———————————————————— ℃), land surface temperature (℃

1018  temperature (———————————————— ℃),The long term mean value and trend are indicated in

1019  the left upper corners. The black lines are annual mean values and the red lines are their 9-yr

1020  running mean values.

1021  Fig. 4. Results from the Preindustrial control experiment. Annual mean time series of the ocean

1022  variables from year 0 to year 500 from top, sea surface salinity (psu); sea water salinity (psu); sea

1023  water temperature (———————————————— ℃); AMOC strength at 26.5N value and trend

1024  are indicated in the left upper corner. The black lines are annual mean values and the red lines are

1025  their 9-yr running mean values.

1026  Fig. 5. Results from the Preindustrial control experiment. The Northern Hemisphere (NH) and

1027  Southern Hemisphere (SH) sea ice extents (SIEs, unit:$10^6$km$^2$) time series year 0 to year 500 in

1028  the Preindustrial control experiment. The black, blue and green lines represent the annual mean,

1029  March and September SIEs, and the red lines are the corresponding 9-yr running mean. The long-

1030  term trends of annual mean SIEs are indicated in the left upper corner of each panel.

1031  Fig. 6. Annual mean outgoing longwave radiation (OLR in units of W m$^{-2}$) derived from

1032  observation (top), the model simulation in the PI experiment (middle) and the model bias

1033  (bottom). The observed OLR filed was derived from the Clouds and the Earth's Radiant Energy

1034  System (CERES) dataset (Loeb et al. 2009).

Fig. 7. The same as in Fig. 6 but for annual mean of SST (°C). The observed SST climatology
was derived from the Hadley Center sea Ice and Sea Surface Temperature (HadISST, Rayner et
al., 2003) for the period of 1870-1880.

Fig. 8. The same as in Fig. 6 except for annual mean of precipitation (mm day$^{-1}$). The observed
precipitation was derived from a Merged precipitation dataset (Lee and Wang 2014), which is the
arithmetic mean of the monthly data from the Global Precipitation Climatology Project (GPCP)
version 2.2 (Adler et al., 2003) and Climate Prediction Center Merged Analysis of Precipitation
(CMAP, Xie and Arkin, 1997).

Fig. 9. Same as in Fig. 6 except for the annual mean sea surface salinity (psu). The observed SSS
data are from the World Ocean Atlas 2009 (WOA09) (Locarnini et al. 2010).

Fig. 10. Results from the abrupt quadrupling $CO_2$ experiment. Global-mean surface air
temperature change relative to the counterpart in the PI experiment. The red and black lines
indicate the results obtained from the NESMv3 and 10 CMIP5 models' MME, respectively.

Fig. 11. Results from the abrupt quadrupling $CO_2$ experiment. The relationships between the
change in the net TOA radiative flux and the global-mean surface air temperature in NESM v3
model. The solid line represents linear least squares regression fit to the 150 years of model
output data. The interception at $\delta T = 0$ indicates the adjusted radiative forcing (F=7.24Wm$^{-2}$). The
slope of the regression line measures the strength of the feedbacks in the climate system, the
climate feedback parameter (-0.981 Wm$^{-2}$K$^{-1}$). The interception at x-axis gives the equilibrium $\delta T$
(7.38 K).

Fig. 12. Results from the abrupt quadrupling $CO_2$ experiment. The relationship between the
change in the global mean radiative fluxes and global mean surface air temperature change. The
climate feedback parameters (Wm$^{-2}$K$^{-1}$) for the TOA longwave clear sky (red), shortwave clear

sky(green), longwave cloud forcing (blue), shortwave cloud forcing (light blue) and net cloud radiative effect (black) are -1.63, 0.675, 0.31, -0.30, 0.02 $Wm^{-2}K^{-1}$, respectively.

Fig. 13. Changes in the surface temperature (top) and precipitation (bottom) derived from the last 30-year climatology in the 150-year abrupt 4 x $CO_2$ experiments. The changes are with reference to the corresponding climatological mean fields from the PI experiment. The right panels show the corresponding zonal mean chnages.

Fig. 14. Results from the 1%per year $CO_2$ increases experiment. Global mean annual surface air temperature change relative to counterpart in the PI experiment. The red and black lines indicate the results obtained from the NESMv3 and 10 CMIP5 models' MME, respectively. The average temperature anomalies between year 60-80 is defined as transit climate sensitivity, which is 2.16K in the NESM v3 model.

|         | TOA net | TOA SW | OLR     | SW CRE  | LW CRE | SST  | LST   | PR   |
|---------|---------|--------|---------|---------|--------|------|-------|------|
| Obs     | 0.83    | 240.51 | -239.68 | -47.16  | 25.98  | 17.2 | 12.58 | 2.68 |
| NESM v3 | 0.2     | 238.65 | -238.45 | -48.44  | 25.75  | 17.7 | 12.72 | 2.86 |

Table 1 Summery of the global averaged annual mean values for radiation (Unit: W m$^{-2}$), temperature(Unit: ℃) and precipitation (mm day$^{-1}$) from last 100-year PI simulation and observations. The observed energy estimations are from CERES ed2.8 on the period of 2001-2014. The observed SST/LST data is derived from Hadley SST/CUR on the period of 1870-1880/1901-1910. The combined CMAP and GPCP precipitation.

1103
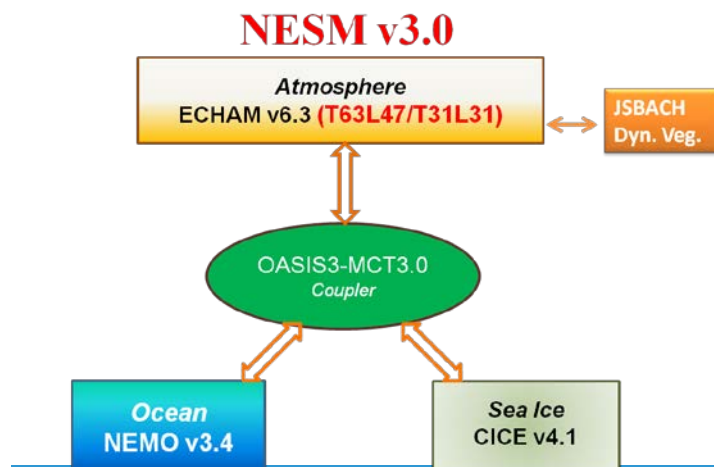
1104

1105

Figure1.Coupled structure of NESM v3 model.

1106

1107

1108

1109

1110

1111

1112

1113
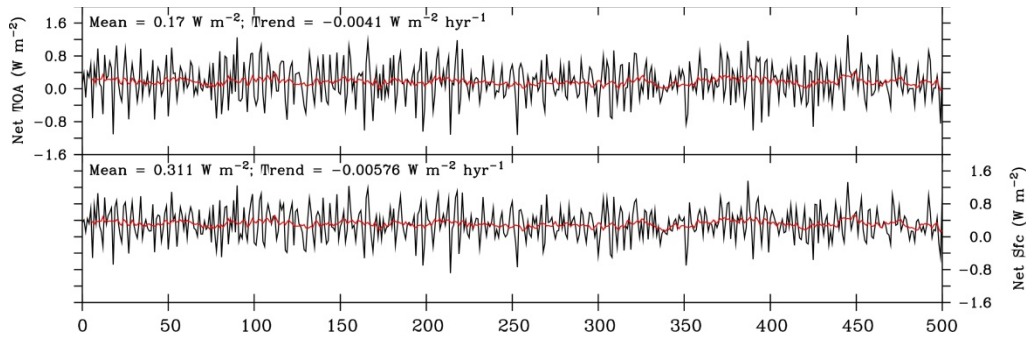
Figure 2 Radiative energy balances in NESM v3. (a) Time series of the net radiative energy fluxes at TOA (downward, W_m⁻², -upper) and (b) the net heat flux at the Earth surface (W_m⁻², bottom², bottom) from year 0 to year 500 in the Preindustrial control experiment. The long-term mean value and trend are indicated in the left upper corner. The black lines indicate annual mean values and the red lines indicate their 9-yr running mean values.
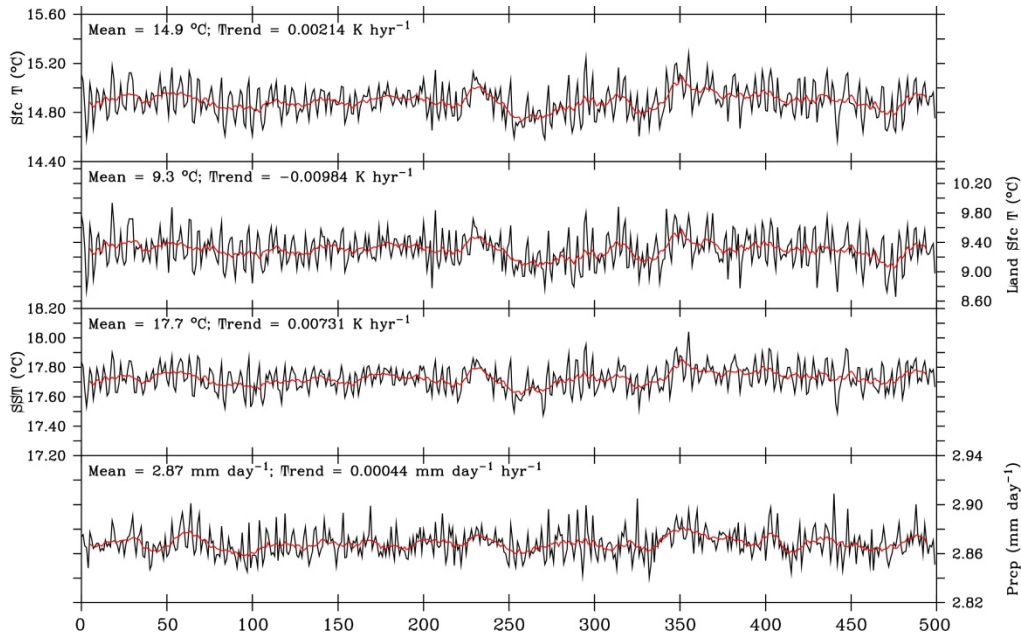
Figure 3 Results from the Preindustrial control experiment. Annual mean time series of the surface temperature and precipitation from year 0 to year 500 in the Preindustrial control experiment, from top, near surface air temperature (℃), land surface temperature (℃), sea surface temperature (℃), and precipitation (mm d$^{-1}$). The long-term mean value and trend are indicated in the left upper corners. The black lines are annual mean values and the red lines are their 9-yr running mean values.
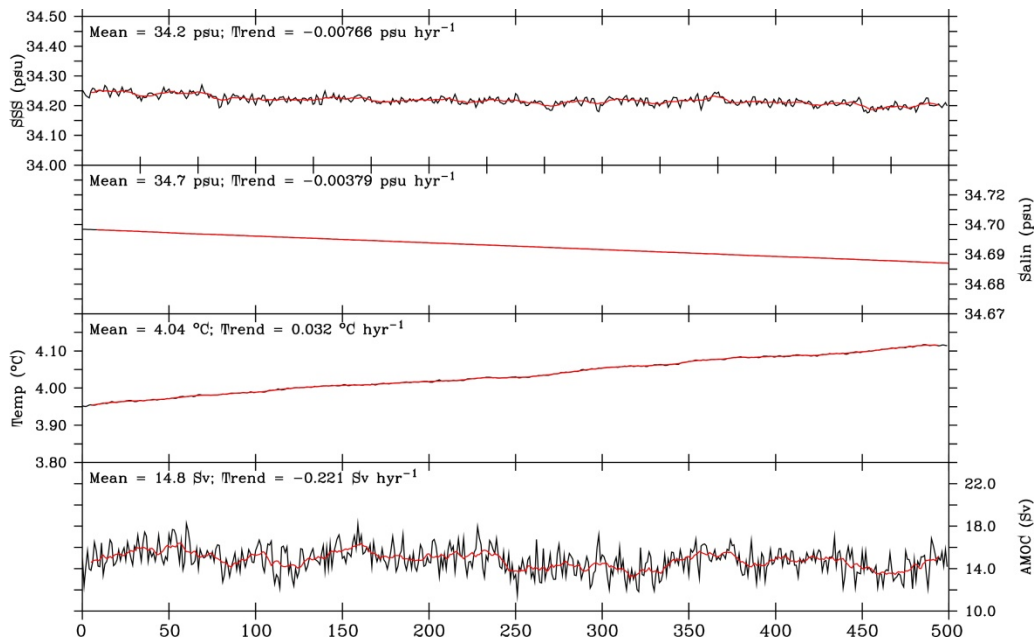
Figure 4 Results from the Preindustrial control experiment. Annual mean time series of the ocean variables from year 0 to year 500 from top, sea surface salinity (psu); sea water salinity (psu); sea water temperature (℃ ), AMOC strength at 26.5°N (sv). The sea water salinity and sea water temperature are the volume-mean values for the full-depth global ocean. The long-term mean value and trend are indicated in the left upper corner. The black lines are annual mean values and the red lines are their 9-yr running mean values.

1169



1170
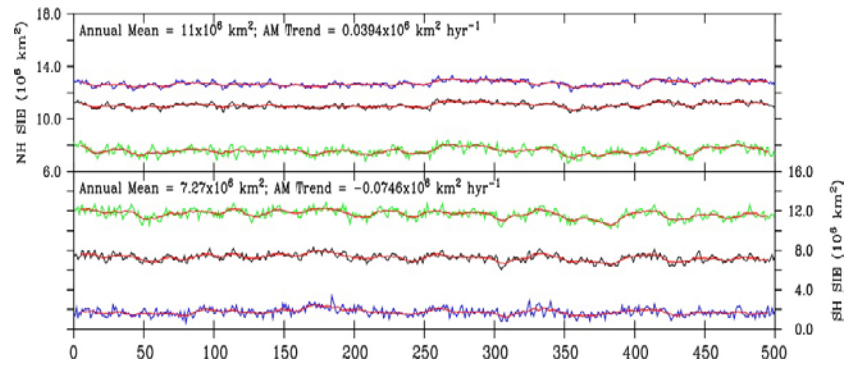
1171    Figure 5 Results from the Preindustrial control experiment. The Northern Hemisphere (NH) and

1172    Southern Hemisphere (SH) sea ice extents (SIEs, unit:$10^6$km$^2$) time series year 0 to year 500 in

1173    the Preindustrial control experiment. The black, blue and green lines represent the annual mean,

1174    March February and September SIEs, and the red lines are the corresponding 9-yr running mean.

1175    The long-term trends of annual mean SIEs are indicated in the left upper corner of each panel.
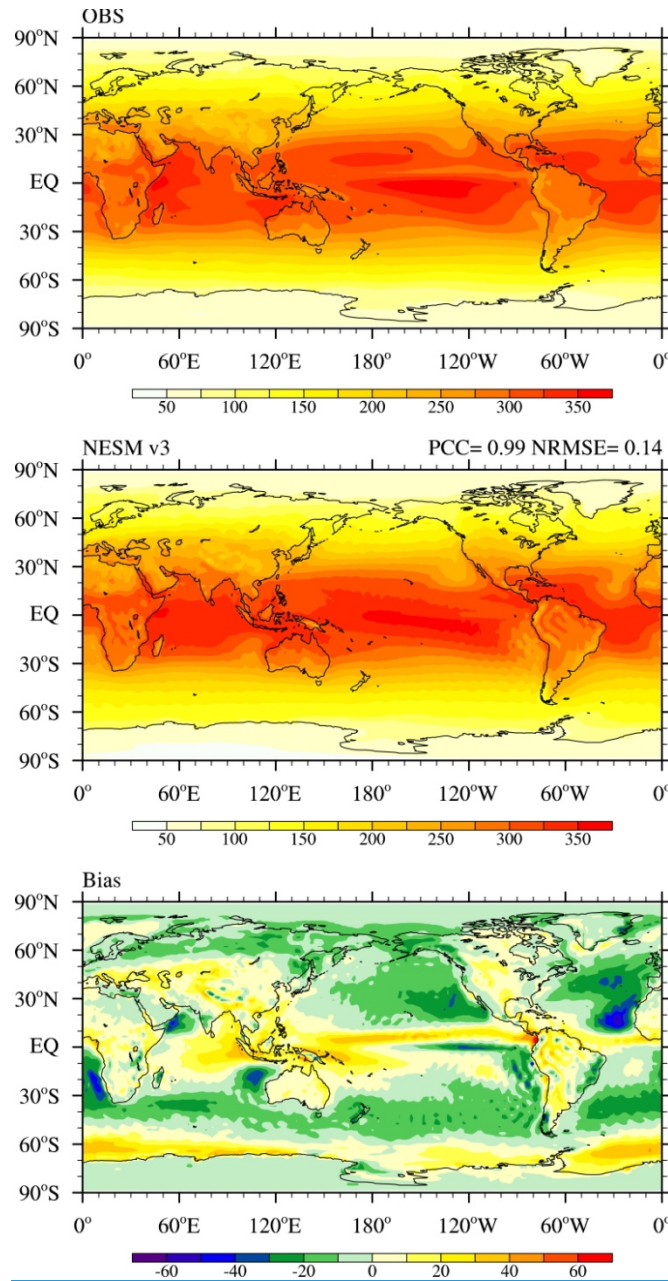
1176

1177

1178

1179

1180

1181

1182

1183

1184

1185

1186

1187

1188

1189

Figure 6  Annual mean  TOA net shortwave radiation ( units: W m$^{-2}$) derived from observation (top), the model simulation in the PI experiment (middle) and the model bias (bottom). The observed radiation ~~feild~~field was derived from the Clouds and the Earth's Radiant Energy System (CERES) dataset (Loeb et al. 2009).

1196

Figure 7 As in Fig. 6 except for~~The same as Figure 6, but for~~ OLR.~~6 Annual mean outgoing~~

~~longwave radiation (OLR in units of W m⁻²) derived from observation (top), the model simulation~~

~~in the PI experiment (middle) and the model bias (bottom). The observed OLR filed was derived~~

~~from the~~ edition 2.8 of ~~Clouds and the Earth's Radiant Energy System (CERES) dataset (Loeb~~

~~et al. 2009).~~

1202

1203

1204

1205

1206
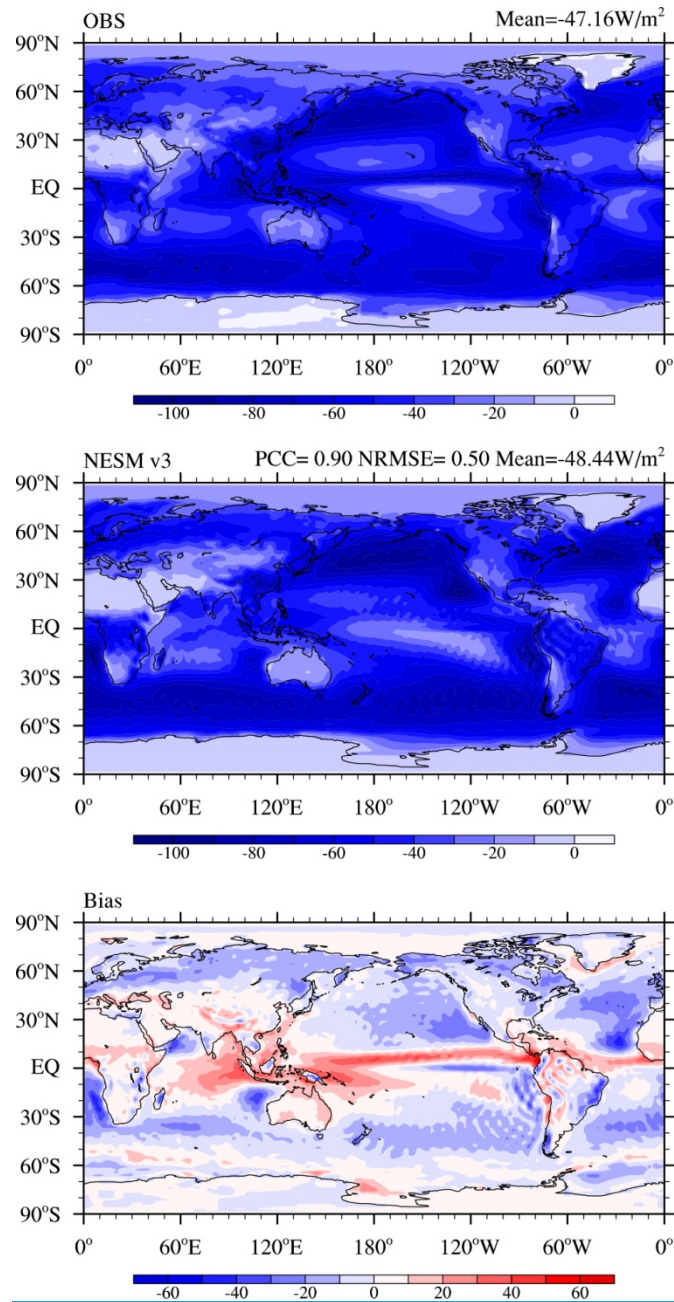
1207      Figure 8 As in Fig. 6 except for~~The same as Figure 6 but for~~ TOA shortwave cloud effect.

1208

1209

1210

1211

1212

1213

Figure 9 As in Fig. 6 except for TOA longwave cloud effect.

1214

1215
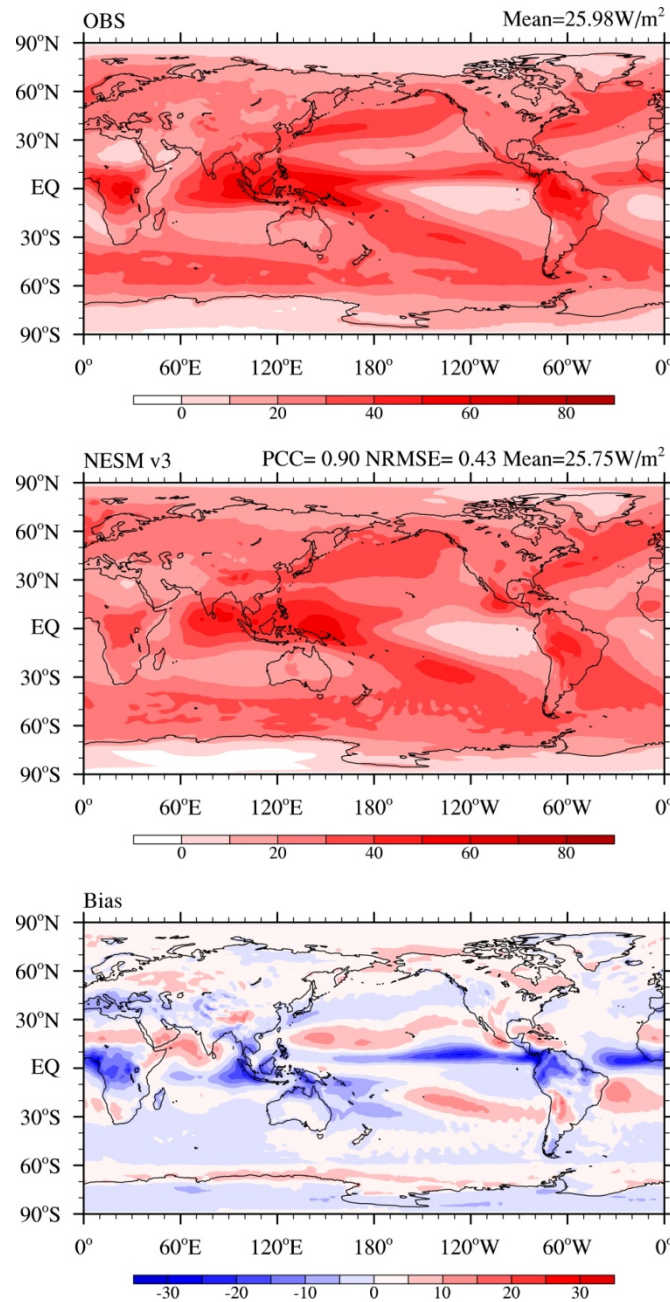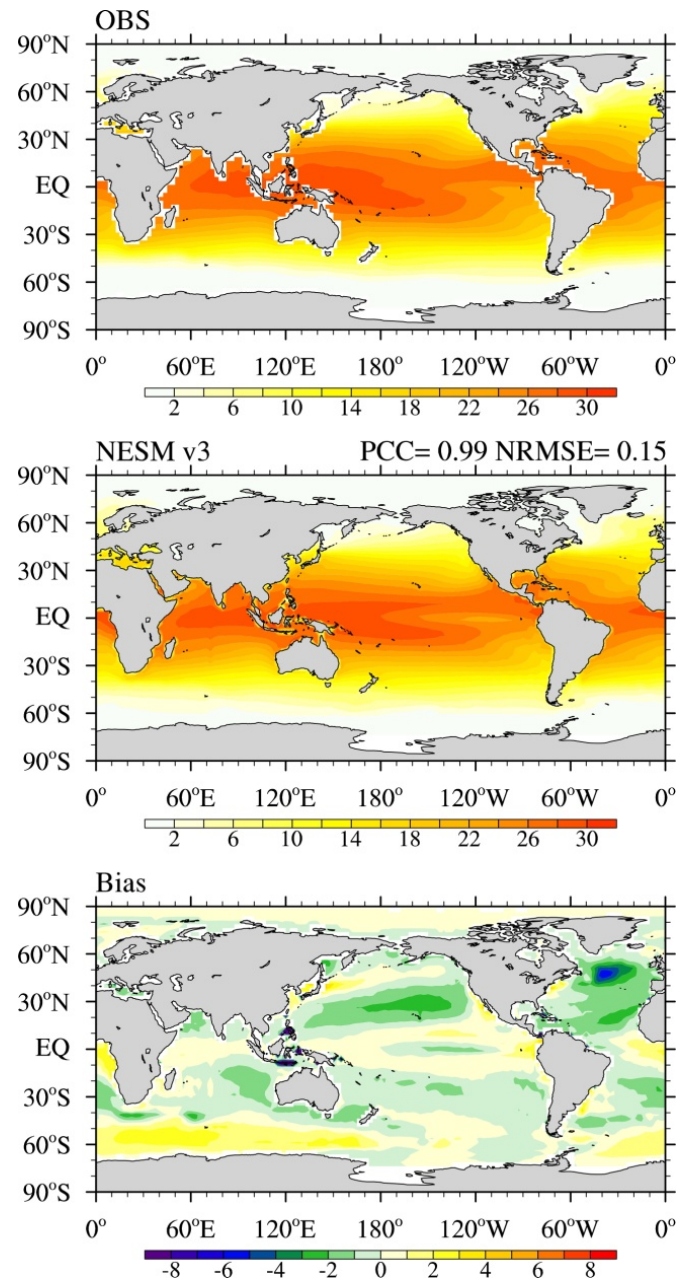
Figure 7 10 As in Fig. 13 except for annual mean of SST (℃). The observed SST climatology

was derived from the Hadley Center sea-Ice and Sea Surface Temperature (HadISST, Rayner et

al., 2003) for the period of 1870-1880.

Figure 11 As in Fig. 10 except ~~The same as Figure 10, but~~ for land surface temperature (℃). The observed land ~~surface climatology~~surface climatology was derived from the CRU-TS-v3.22 (Harris et al. 2014) for the period of 1901-1910.

1226
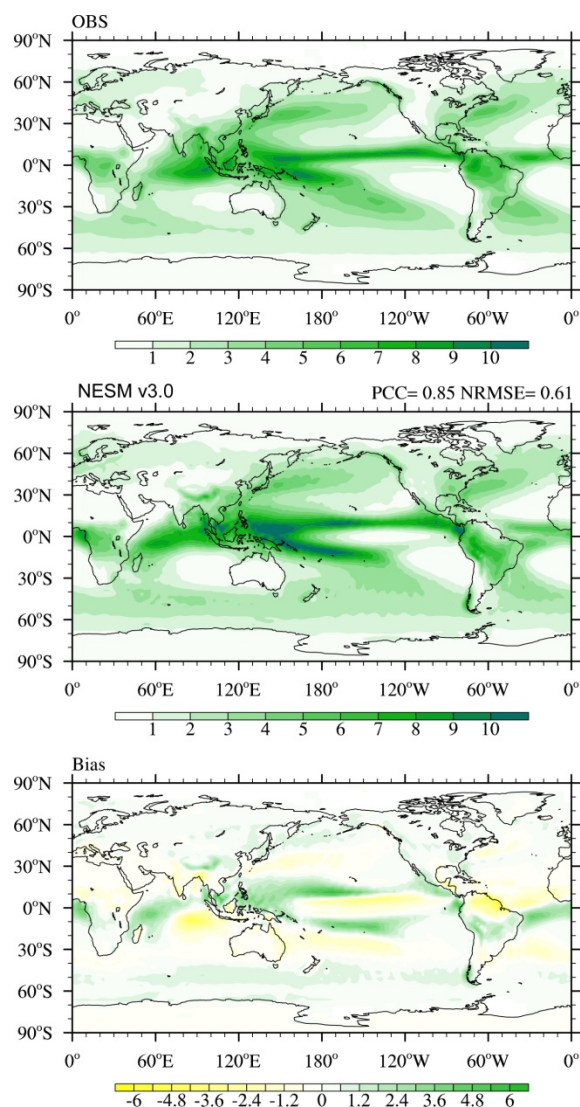


1227

1228    Figure 8 12 The same as in Fig. 6 except for annual mean of precipitation (mm day$^{-1}$). The

1229    observed precipitation was derived from a Merged precipitation dataset (Lee and Wang 2014),

1230    which is the arithmetic mean of the monthly data from the Global Precipitation Climatology

1231    Project (GPCP) version 2.2 (Adler et al., 2003) and Climate Prediction Center Merged Analysis

1232    of Precipitation (CMAP, Xie and Arkin, 1997).

1233

1234

1235

1236
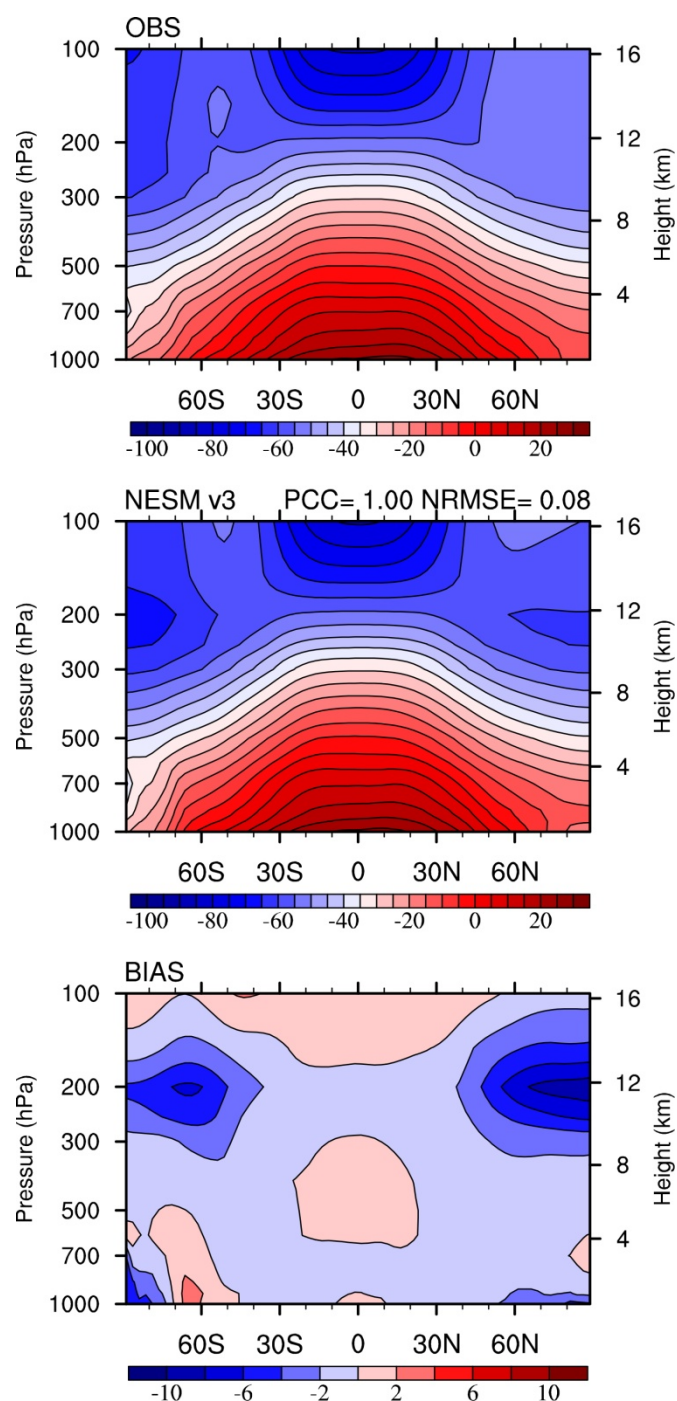


1237

1238  Figure 13 The zonal mean climatological of temperature in NESM v3, ERA-interim (1979-2008)

1239  and model bias.

1240

1241
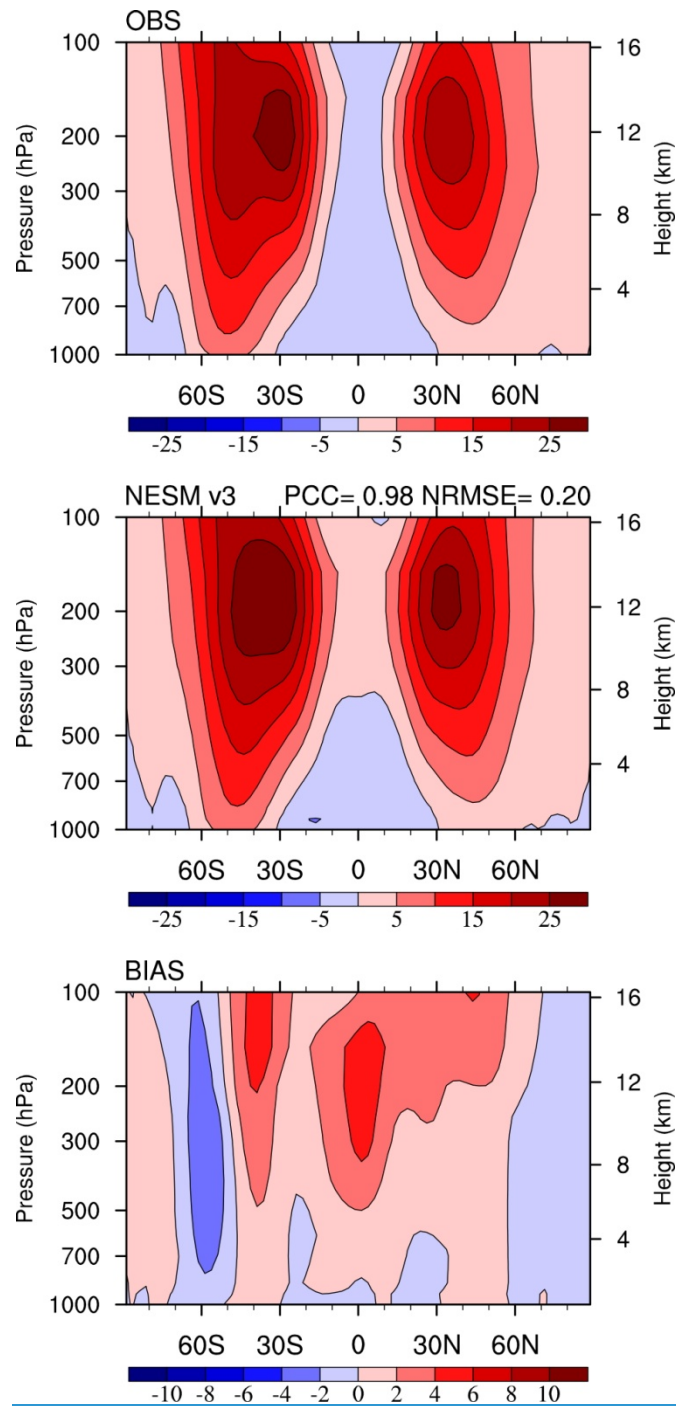
Figure 14 As in Fig. 13 except for zonal wind.The same as Figure 13, except for zonal wind.

1242

1243

1244

1245

1246
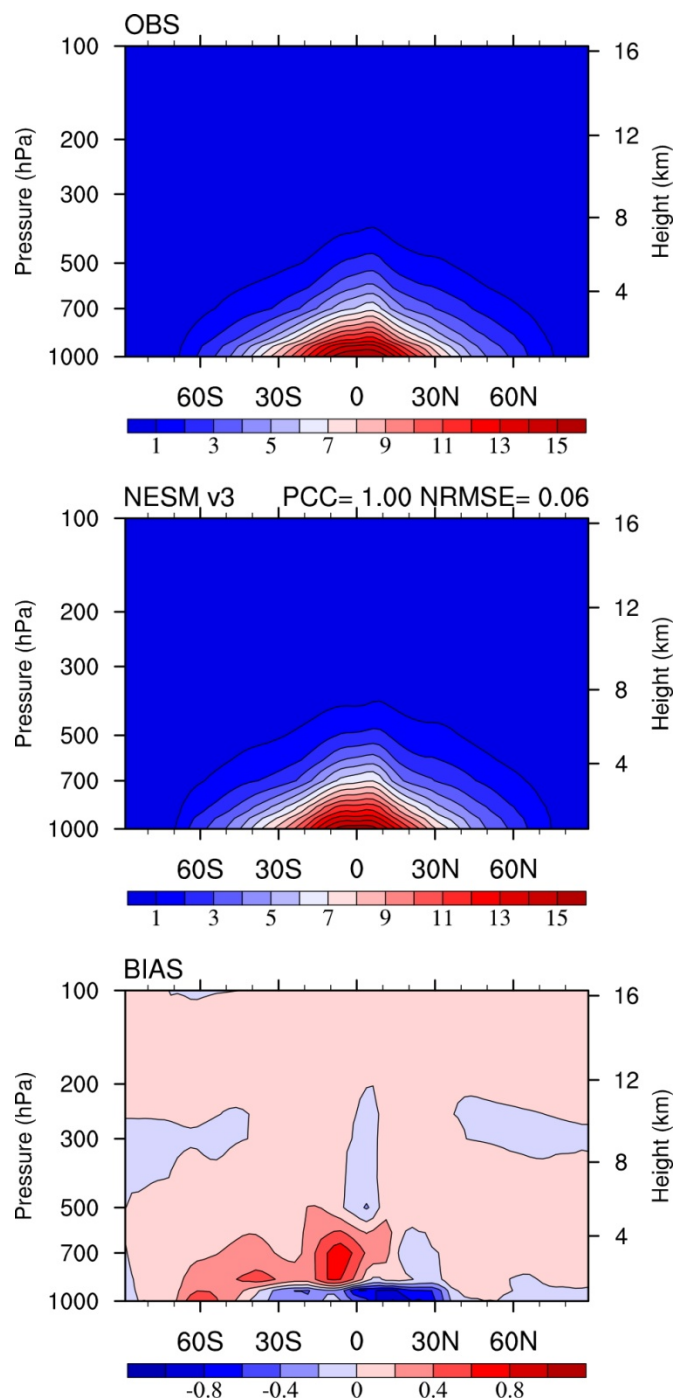
Figure 15 As in Fig. 143 except for specific humidtyhumidity.

1248

1249
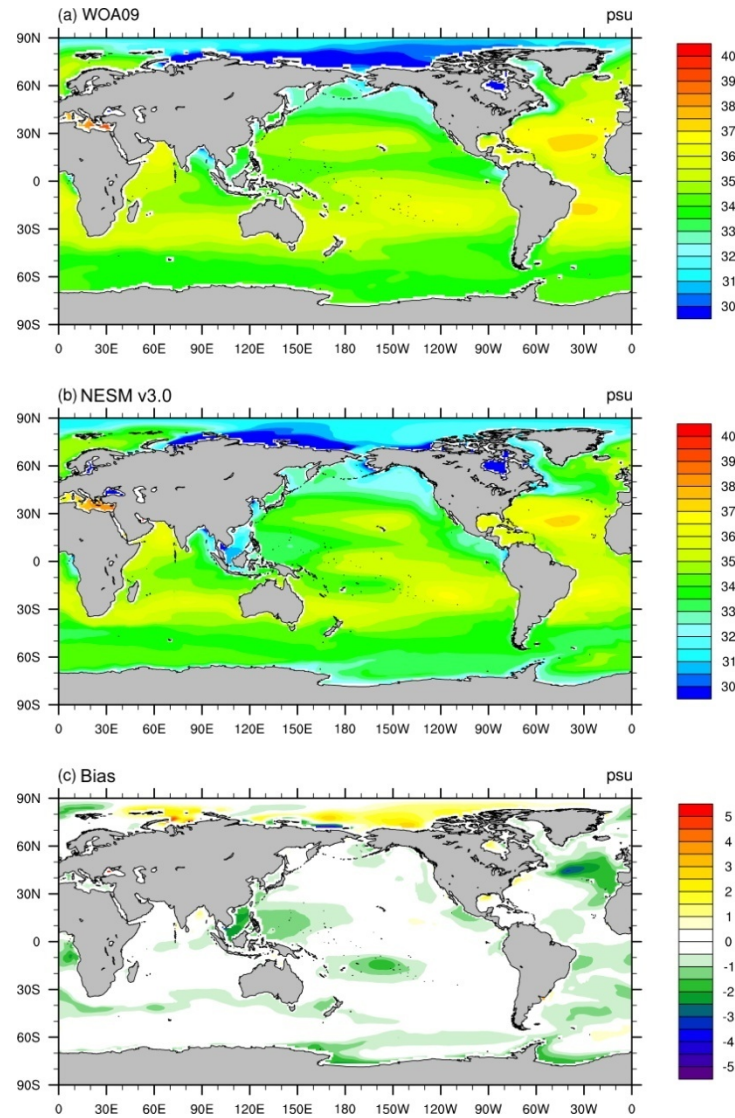
Figure 169 Same as in Fig. 6 except for the annual mean sea surface salinity (psu). The observed

SSS data are from the World Ocean Atlas 2009 (WOA09) (Locarnini et al. 2010).

1250

1251

1252

1253

1254

1255

1256

1257

1258

1259
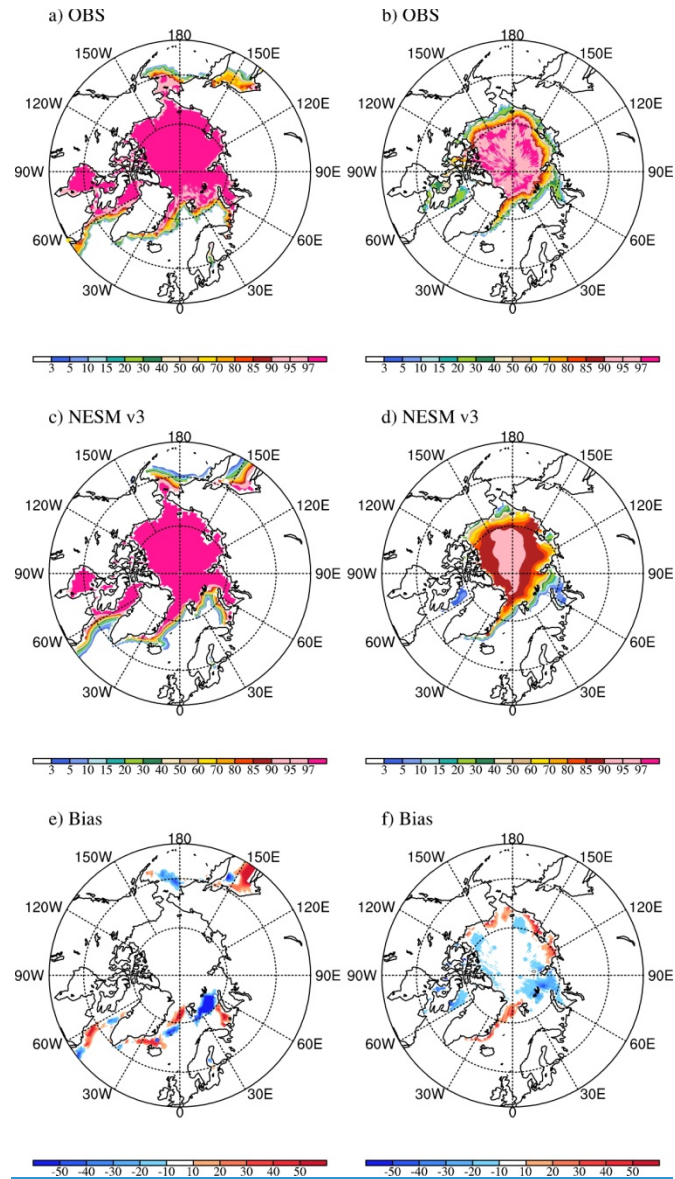
Figure 17 Climatological Arctic sea ice concentration in NESM v3 (upper), HadISST (middle),
and model bias (bottom) for February (a,c,e) and September(b,d,f). The observed sea ice
concentration is averaged over the period of 1870-1880.

1263

1264

1265

1266

1267

1268    Figure 18 As in Fig. 17 except for Antarctic.

1269

1270

1271

1272

1273



1274
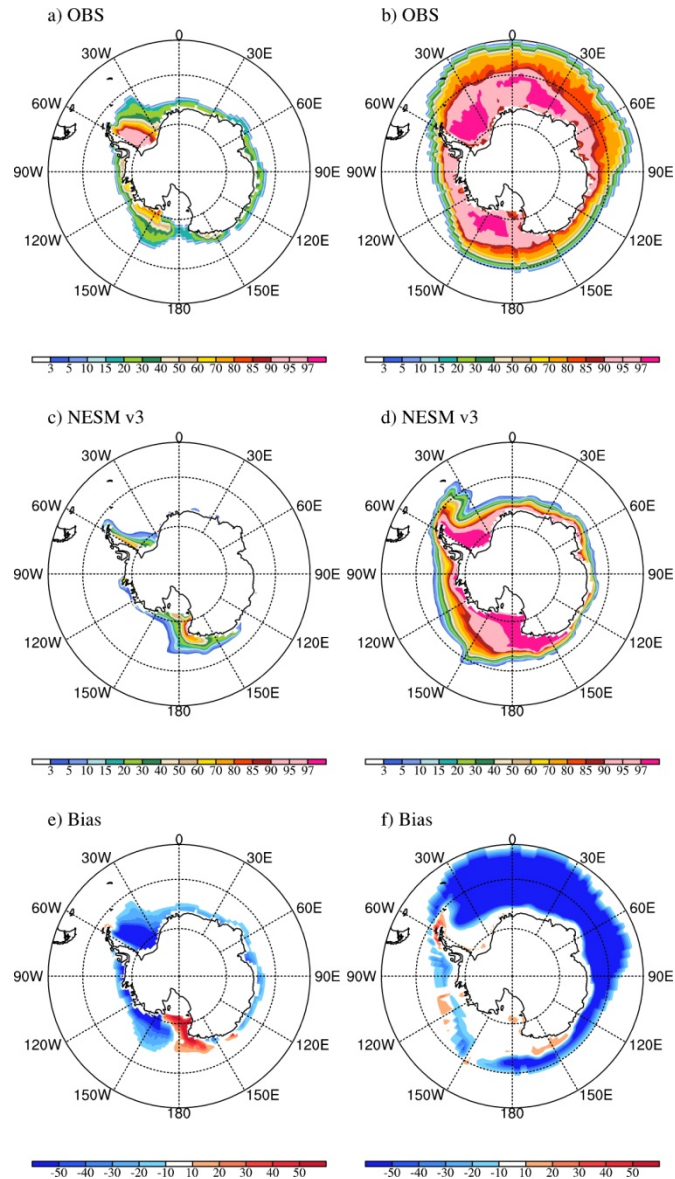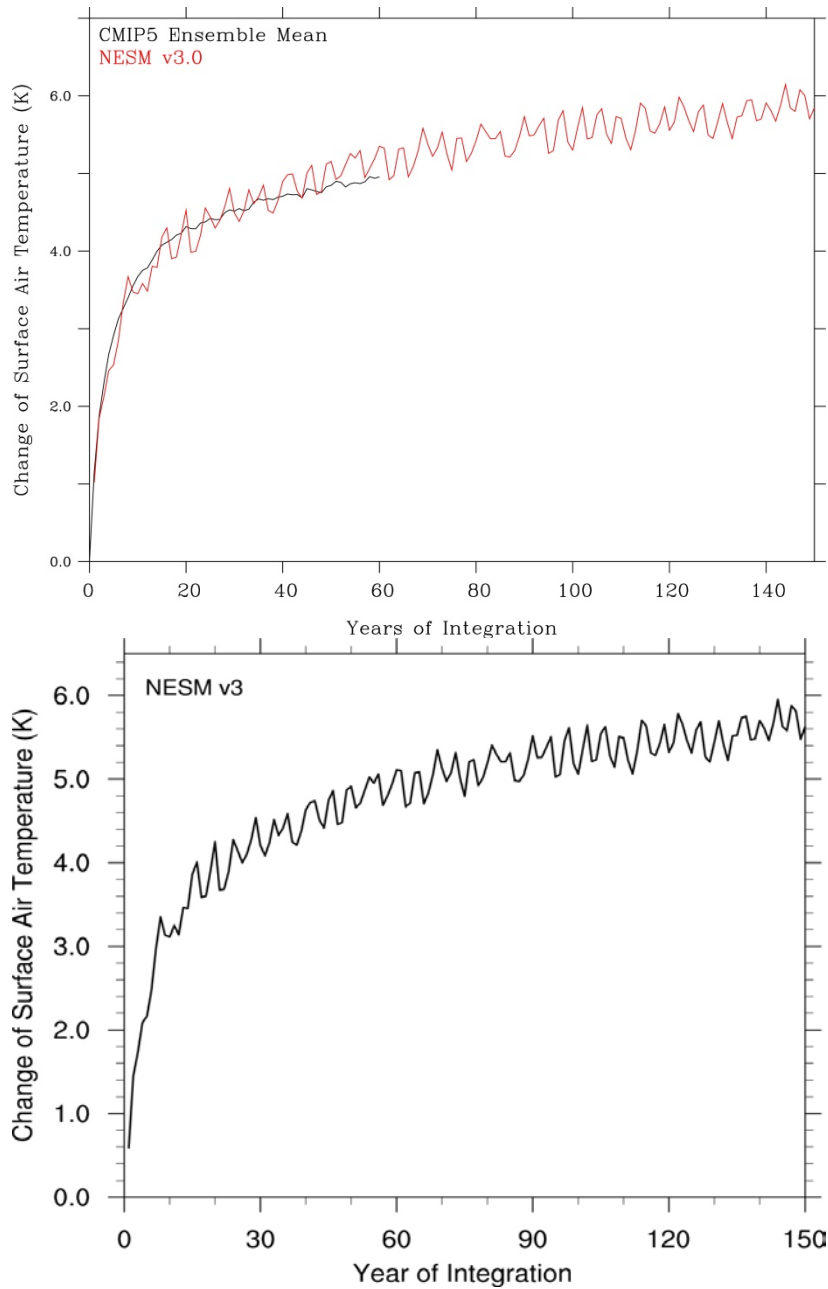
1275      Figure ~~10~~ 19 Results from the abrupt quadrupling $CO_2$ experiment. Global-mean surface air

1276      temperature change relative to the counterpart in the PI experiment. ~~The red and black lines~~

1277      ~~indicate the results obtained from the NESMv3 and 10 CMIP5 models' MME, respectively.~~

1278

1279

1280

1281

1282

1283

1284

1285

1286

1287

1288

1289

1290
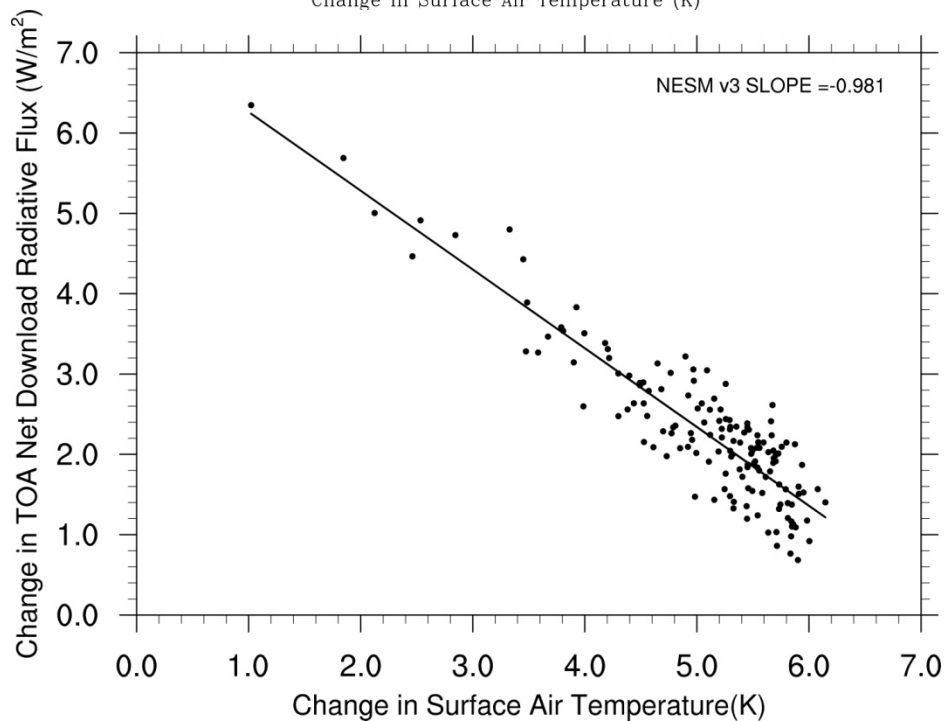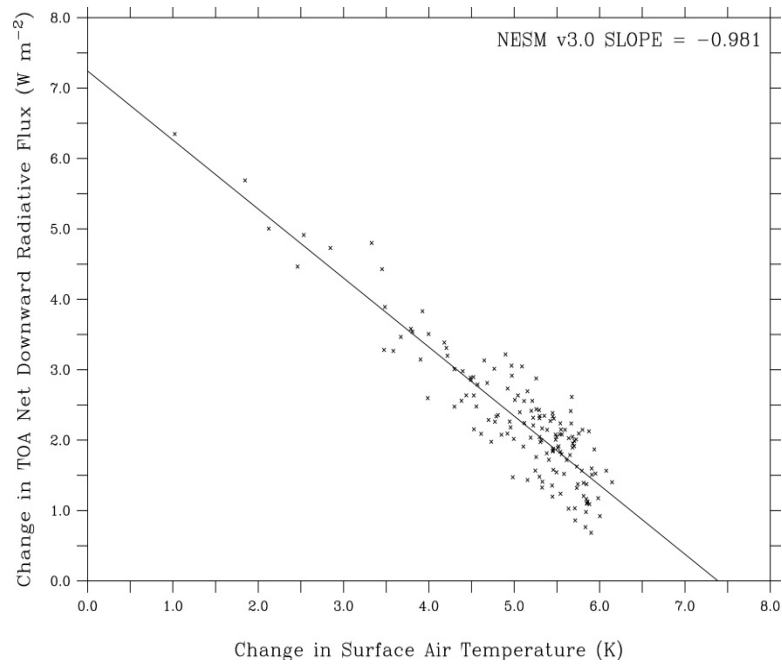
1291



1292

1293 Figure ~~11~~ 20 Results from the abrupt quadrupling $CO_2$ experiment. The relationships between the

1294 change in the net TOA radiative flux and the global-mean surface air temperature in NESM v3

1295 model. The solid line represents linear least squares regression fit to the 150 years of model

1296 output data. The interception at $\delta T = 0$ indicates the adjusted radiative forcing (F=7.24Wm$^{-2}$). The

1297 slope of the regression line measures the strength of the feedbacks in the climate system, the

1298    climate feedback parameter (-0.981 $Wm^{-2}K^{-1}$). The interception at x-axis gives the equilibrium $\delta T$

1299    (7.38 K).

1300
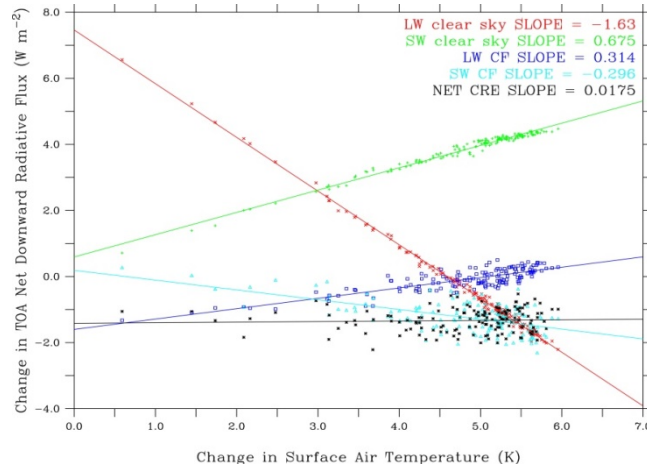
1301

1302

1303

1304

1305

1306
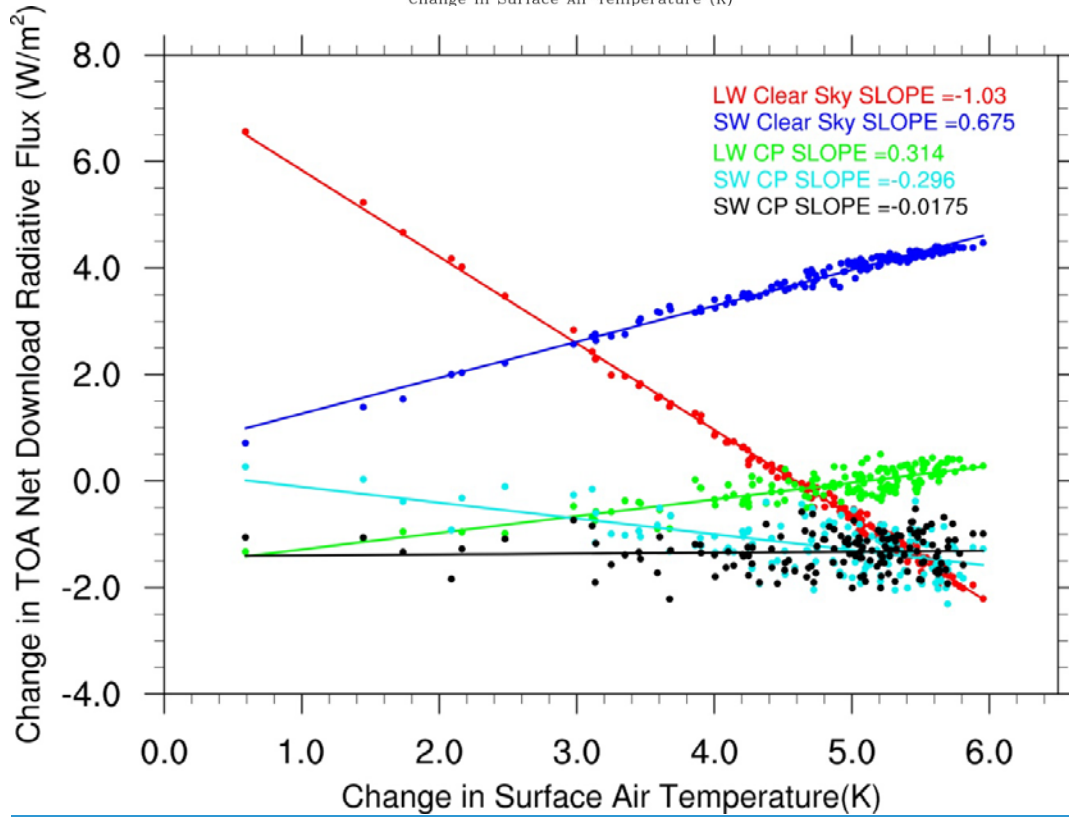
1307



1308

Figure 21~~12~~ Results from the abrupt quadrupling $CO_2$ experiment. The relationship between the

change in the global mean radiative fluxes and global mean surface air temperature change. The

climate feedback parameters ($Wm^{-2}K^{-1}$) for the TOA longwave clear sky (red), shortwave clear

sky(green), longwave cloud forcing (blue), shortwave cloud forcing (light blue) and net cloud

radiative effect (black) are -1.63, 0.675, 0.31, -0.30, 0.02 $Wm^{-2}K^{-1}$, respectively.

1314

1315
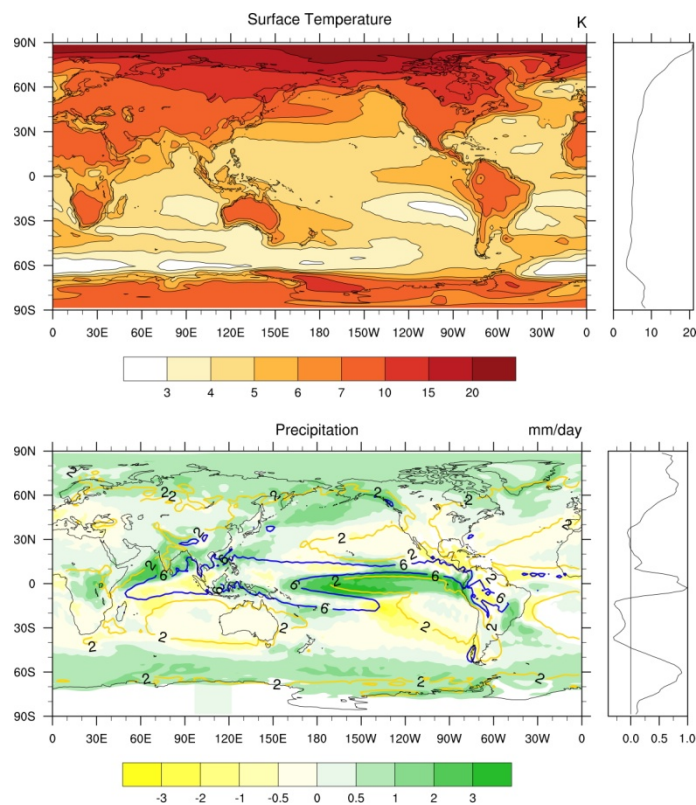


1316

1317 Figure 2213 Changes in the surface temperature (top) and precipitation (bottom) derived from the

1318 last 30-year climatology in the 150-year abrupt 4 x $CO_2$ experiments. The changes are with

1319 reference to the corresponding climatological mean fields from the PI experiment. The right

1320 panels show the corresponding zonal mean changes.
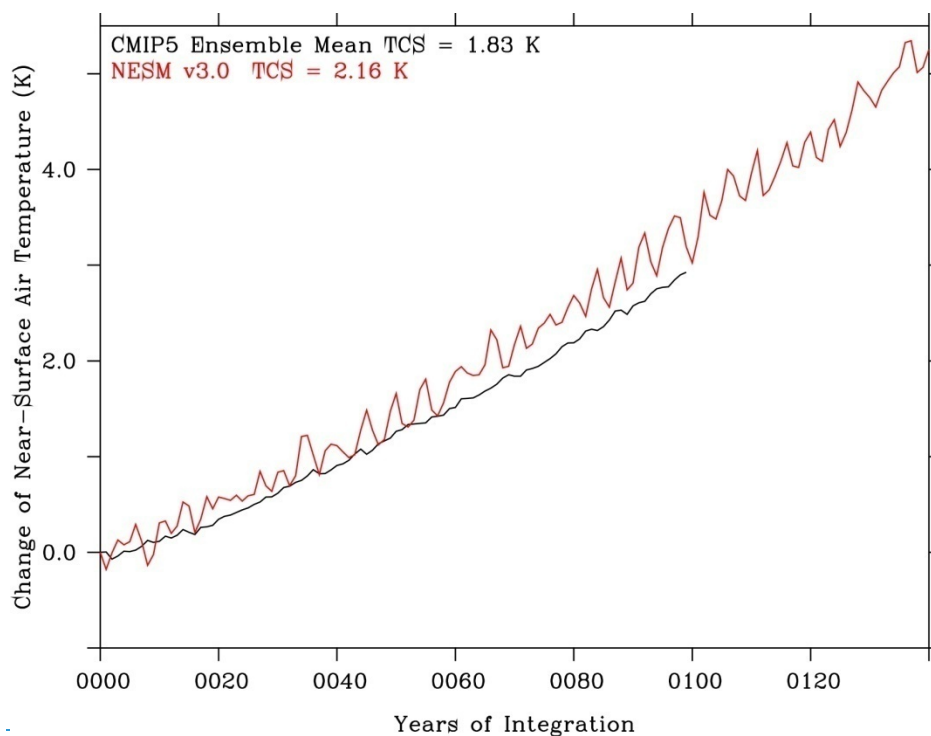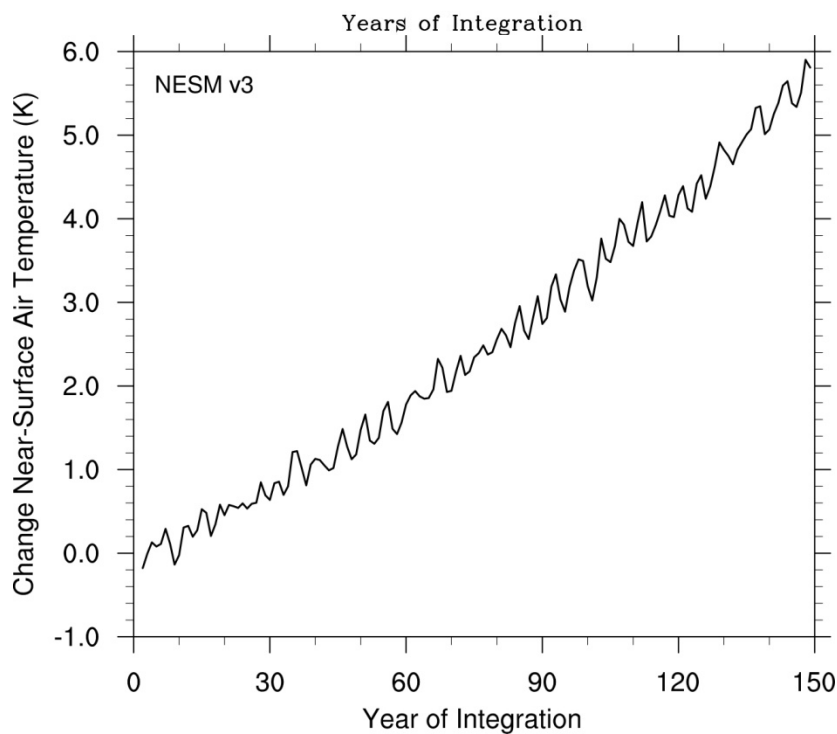
1321

1322

1323

1324

1325

1326

1327

1328

1332  Figure 2314 Results from the 1%per year $CO_2$ increases experiment. Global mean annual surface

1333  air temperature change relative to counterpart in the PI experiment. ~~The red and black lines~~

1334  ~~indicate the results obtained from the NESMv3 and 10 CMIP5 models' MME, respectively.~~ The

1335    average temperature anomalies between year 60-80 is defined as transit climate sensitivity, which

1336    is 2.16K in the NESM v3 model.